


2011

Molybdenum Nitride Films in the Back Contact Structure of Flexible Substrate CdTe Solar Cells

Vasudha Guntur

University of South Florida, vguntur@mail.usf.edu

Follow this and additional works at: <http://scholarcommons.usf.edu/etd>

 Part of the [American Studies Commons](#), and the [Electrical and Computer Engineering Commons](#)

Scholar Commons Citation

Guntur, Vasudha, "Molybdenum Nitride Films in the Back Contact Structure of Flexible Substrate CdTe Solar Cells" (2011). *Graduate Theses and Dissertations*.

<http://scholarcommons.usf.edu/etd/3136>

This Thesis is brought to you for free and open access by the Graduate School at Scholar Commons. It has been accepted for inclusion in Graduate Theses and Dissertations by an authorized administrator of Scholar Commons. For more information, please contact scholarcommons@usf.edu.

Molybdenum Nitride Films in the Back Contact Structure of Flexible Substrate CdTe
Solar Cells

by

Vasudha Guntur

A thesis submitted in partial fulfillment
of the requirements for the degree of
Master of Science in Electrical Engineering
Department of Electrical Engineering
College of Engineering
University of South Florida

Major Professor: Chris Ferekides, Ph.D.
Don Morel, Ph.D.
Andrew Hoff, Ph.D.

Date of Approval:
March 14, 2011

Keywords: Diffusion Barrier, MoN, Reactive Sputtering, δ -MoN, Amorphous Barrier

Copyright © 2011, Vasudha Guntur

DEDICATION

I dedicate this thesis to my parents: Mr. G. V. Raghava Rao and Mrs G. Vara Lakshmi, grandparents: Mr. G. Venkateswarlu and Mrs G. Adi Lakshmi and my younger brother G. Santosh Nath for your constant support both financially and emotionally.

ACKNOWLEDGMENTS

I would like to thank my Professor Dr. Chris Ferekides for his support and guidance in my research work. I would like to thank my committee members Drs. Don Morel and Andrew Hoff for accommodating me irrespective of their busy schedules and providing me constructive feedback in this work. I want to thank my research group: Vasilios Palekis, Ryan Anders, Kartikay Singh, Ranjit Rudraraju and Anand Kumar Chiluka for their support. I thank my parents Mr. G. V. Raghava Rao and Mrs. G. Vara Lakshmi, grand-parents Mr. G. Venkateswarlu and Mrs. G. Adi Lakshmi and my younger brother Mr. G. Santosh Nath for being a great support to me all throughout my research.

TABLE OF CONTENTS

| | |
|---|-----|
| LIST OF TABLES | iii |
| LIST OF FIGURES | iv |
| ABSTRACT | vi |
| CHAPTER 1: INTRODUCTION | 1 |
| Energy Consumption and Renewable Sources of Energy | 1 |
| Solar Cell Generations and Limits to Efficiency | 3 |
| Solar Cell Operation | 7 |
| Solar Spectrum for Terrestrial Applications | 11 |
| Purpose and Content of This Thesis | 12 |
| CHAPTER 2: METAL SEMICONDUCTOR CONTACTS | 13 |
| The Schottky – Mott Theory | 13 |
| Contacts to an N-type Semiconductor | 14 |
| Contacts to a P-type Semiconductor | 14 |
| The Bardeen Model | 16 |
| Ohmic Metal-Semiconductor Contacts | 17 |
| Doping the Semiconductor | 17 |
| Intermediate Layers | 18 |
| Adding Recombination Centers | 19 |
| Modifying the Fermi Level Pinning at the Metal-Semiconductor Interface | 19 |
| CHAPTER 3: THIN FILM CADMIUM TELLURIDE SOLAR CELLS | 20 |
| Cadmium Telluride Solar Cells | 20 |
| Superstrate CdTe Solar Cells | 20 |
| Substrate CdTe Solar Cells on Flexible Substrates | 22 |
| Challenges in Substrate CdTe Solar Cells | 23 |
| CHAPTER 4: BACK CONTACTS TO CADMIUM TELLURIDE SOLAR CELLS | 24 |
| History of Back Contacts to Cadmium Telluride Solar Cells | 24 |
| Metal Contacts to P-type CdTe | 24 |
| P+ Doping of CdTe | 25 |
| Interlayers between CdTe and the Metal Contact | 26 |

| | |
|---|----|
| History of Back Contacts to Substrate Cadmium Telluride Solar Cells | 28 |
| CHAPTER 5: MOLYBDENUM NITRIDE | 29 |
| Transition Metal Nitrides | 29 |
| Crystal Structure of Molybdenum Nitride | 29 |
| Structural and Mechanical Properties of Molybdenum Nitride | 32 |
| CHAPTER 6: CHARACTERIZATION METHODS AND EXPERIMENTAL PROCEDURE..... | 35 |
| Four-point Probe | 35 |
| X-Ray Diffraction Spectroscopy (XRD) | 36 |
| Energy Dispersive X-ray Spectroscopy (EDS) Analysis..... | 38 |
| Scanning Electron Microscopy (SEM) | 39 |
| RF Magnetron Sputtering | 39 |
| Experimental Procedure..... | 42 |
| Sample Preparation | 42 |
| The Vacuum System..... | 42 |
| Spectral Response Measurement | 43 |
| J-V Measurement | 44 |
| CHAPTER 7: MOLYBDENUM NITRIDE FILMS AND SOLAR CELLS | 45 |
| Molybdenum and Molybdenum Nitride Thin Films by RF Magnetron Sputtering..... | 45 |
| Thin Film Characterization..... | 45 |
| Rate of Deposition and Resistivity for Molybdenum Nitride Thin Films | 45 |
| X-Ray Diffraction Spectroscopy (XRD) Analysis | 49 |
| Energy Dispersive X-ray Spectroscopy (EDS) Analysis..... | 53 |
| Scanning Electron Microscopy (SEM) Analysis | 55 |
| Solar Cells with Molybdenum Nitride Back Contacts..... | 57 |
| J-V measurements with and without Molybdenum Nitride Back Contacts..... | 58 |
| Spectral Response Measurements of CdTe Solar Cells with Molybdenum Nitride in the Back Contact Structure. | 64 |
| Solar Cell Efficiency..... | 64 |
| Work Function of Mo-N | 65 |
| Nitrogen Incorporation into CdTe | 65 |
| CHAPTER 8: CONCLUSIONS AND FUTURE WORK..... | 66 |
| Conclusions..... | 66 |
| Future Work | 67 |
| REFERENCES | 69 |

LIST OF TABLES

| | |
|--|----|
| Table 7.1: Resistivity of Mo-N films deposited at 250W with increasing N ₂ : Ar ratio | 47 |
| Table 7.2: Resistivity of Mo-N films deposited at 300W with increasing N ₂ : Ar ratio | 47 |
| Table 7.3: Crystal parameters of various phases of Molybdenum Nitride | 53 |
| Table 7.4: Composition of films determined by EDS..... | 54 |
| Table 7.5: Comparison of performance of solar cells with Mo and MoN back contacts | 59 |
| Table 7.6: Solar cell characteristics for varying N ₂ for cells with ‘SS/Mo/Mo- N/CdTe/CdS/SnO ₂ /ITO’ configuration..... | 61 |
| Table 7.7: Solar cell characteristics for varying N ₂ for cells with the stack as back contact..... | 63 |

LIST OF FIGURES

| | |
|---|----|
| Figure 1.1 World energy consumption by type of energy source in year 2008 [1] | 2 |
| Figure 1.2 World photovoltaic production from 1990 to 2008 [4] | 3 |
| Figure 1.3 Efficiencies and costs for the three solar cell generations [7] | 5 |
| Figure 1.4 Best research-cell efficiencies [9] | 6 |
| Figure 1.5 Theoretical PV efficiency vs. experimental PV performance [10] | 7 |
| Figure 1.6 Working of a p-n junction solar cell..... | 8 |
| Figure 1.7 Equivalent circuit of an ideal solar cell [11] | 9 |
| Figure 1.8 I-V characteristics of an ideal solar cell [11]..... | 10 |
| Figure 1.9 Solar spectra for AM 1.5, AM0 and 5800K black body [12]..... | 11 |
| Figure 2.1 Energy band diagrams of metal and n-type semiconductor contacts [12], [15] | 15 |
| Figure 2.2 Energy band diagrams of metal and p-type semiconductor contacts [12], [15] | 16 |
| Figure 2.3 Carrier flow based on increasing dopant concentration for a depleting n-type metal-semiconductor contact [15] | 18 |
| Figure 3.1 Predicted efficiency versus band gap for thin film solar cells [21]..... | 21 |
| Figure 3.2 Basic superstrate CdTe solar cell configuration..... | 22 |
| Figure 3.3 Basic substrate CdTe solar cell structure..... | 23 |
| Figure 5.1 Molybdenum – nitrogen phase diagram [60] | 30 |

| | |
|---|----|
| Figure 5.2 Crystal structure of β -Mo ₂ N [64] | 31 |
| Figure 5.3 Crystal structure of γ Mo ₂ N [64] | 32 |
| Figure 5.4 Crystal structure of δ -MoN [69] | 32 |
| Figure 6.1 Four-point probe [15] | 36 |
| Figure 6.2 Bragg diffraction from adjacent crystal planes | 37 |
| Figure 6.3 X-ray emission recorded for EDS [15] | 39 |
| Figure 6.4 Schematic of magnetron sputtering [74] | 41 |
| Figure 6.5 Vacuum system schematic | 42 |
| Figure 7.1 Rate of deposition for Mo-N with increasing N ₂ /Ar ratio | 46 |
| Figure 7.2 Resistivity of Mo-N with increasing N ₂ /Ar ratio | 49 |
| Figure 7.3 XRD spectra of Mo and Mo-N films deposited at 300W | 52 |
| Figure 7.4 XRD spectra of Mo-N films deposited at 250W | 53 |
| Figure 7.5 Variation of atomic percentage of Mo, N and O by EDS | 54 |
| Figure 7.6 SEM images of Mo and Mo-N films | 56 |
| Figure 7.7 J-V curves for solar cells with Mo versus Mo/MoN for the back contact | 59 |
| Figure 7.8 J-V curves for solar cells with varying N ₂ and Ar pressures | 61 |
| Figure 7.9 J-V measurements of solar cells with Mo-N/Mo/Mo-N and Mo/Mo- N/Mo stack used as back contacts. | 63 |
| Figure 7.10 SR curves of solar cells with Mo and Mo/Mo-N used as back contacts. | 64 |

ABSTRACT

CdTe solar cells in the superstrate configuration have achieved record efficiencies of 16% but those in the substrate configuration have reached efficiencies of only 7.8%. A major reason for the lower efficiency of substrate CdTe solar cells is the poor back contact. In this work, CdTe solar cells of the substrate configuration have been fabricated on flexible metallic substrates. For this type of devices, impurity diffusion out of stainless-steel substrates due to high temperature processing can be a cause for poor cell performance. It is necessary to investigate ways of improving the back contact by trying to mitigate the above factors. In this work, Nitrogen has been incorporated in Molybdenum by RF magnetron sputtering. Nitrogen incorporation has helped achieve a 2% increase in efficiency for the best cell and an improvement of 1.5% on an average.

CHAPTER 1:

INTRODUCTION

Energy Consumption and Renewable Sources of Energy

With the ever increasing demand for energy, exploiting natural resources for energy production and consumption has come to be of paramount importance. A major portion of today's energy demands are met by fossil fuels, which account for about 85% of the current world energy consumption, with nuclear energy supplying about 5% and renewable energy catering to about 10% of today's energy needs, Figure 1.1 [1]. If we continue consuming fossil fuels at the rate we do currently, we would be exhausted of oil in less than 45.7 years, natural gas in about 62.8 years and coal in 119 years [2]; and these figures are without considering the yearly increase in consumption.

Combustion of fossil fuels poses a threat to the climate on earth due to the emission of CO₂ and other harmful gases and due to oil leaks, such as the BP leak in the Gulf of Mexico (2010). Carbon sequestration has helped mitigate CO₂ release to the atmosphere but poses a challenge of finding huge secure storage spaces: storing the 25 billion tons of CO₂ produced annually would require 12,000 km³ [3].

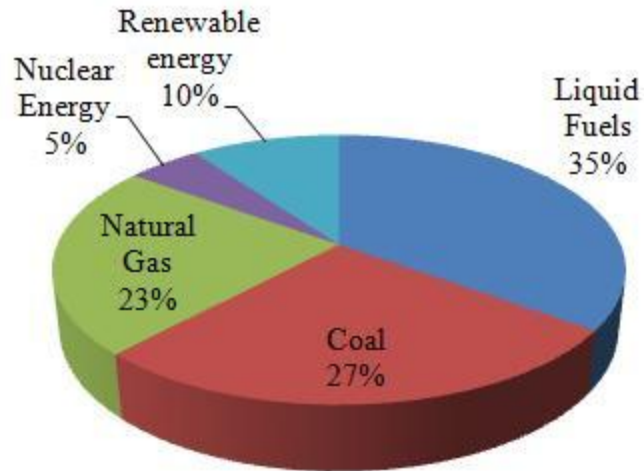


Figure 1.1 World energy consumption by type of energy source in year 2008 [1]

The current world energy consumption is 13 TW and is expected to reach a whopping 30 TW by 2050 [3]. It is hence imperative to replace fossil fuels and other non-renewable hazardous energy sources with renewable and clean sources of energy. Tidal, geothermal, hydroelectric and wind energy together can account for only a small percentage of the total energy consumption on our planet. Production of nuclear power even in the most efficient way feasible: constructing a 1GW_e nuclear power plant every other day, would cause the uranium resources to be exhausted in 10 years and would generate only 2TW when compared to the world consumption of 13TW [3]. “*More energy from sunlight ($4.3 \times 10^{20} \text{ J}$) strikes the earth in one hour, than all the energy consumed on the planet in a year ($4.1 \times 10^{20} \text{ J}$)*”, this suggests the huge untapped potential for commercial energy production utilizing the sun’s energy [3].

Solar Cell Generations and Limits to Efficiency

Solar cells are a direct means to convert sunlight to electrical energy. Solar cell production has been increasing at a steady rate every year: production has been increasing by a factor of 20% from 2005- 2008, Figure 1.2 [4].

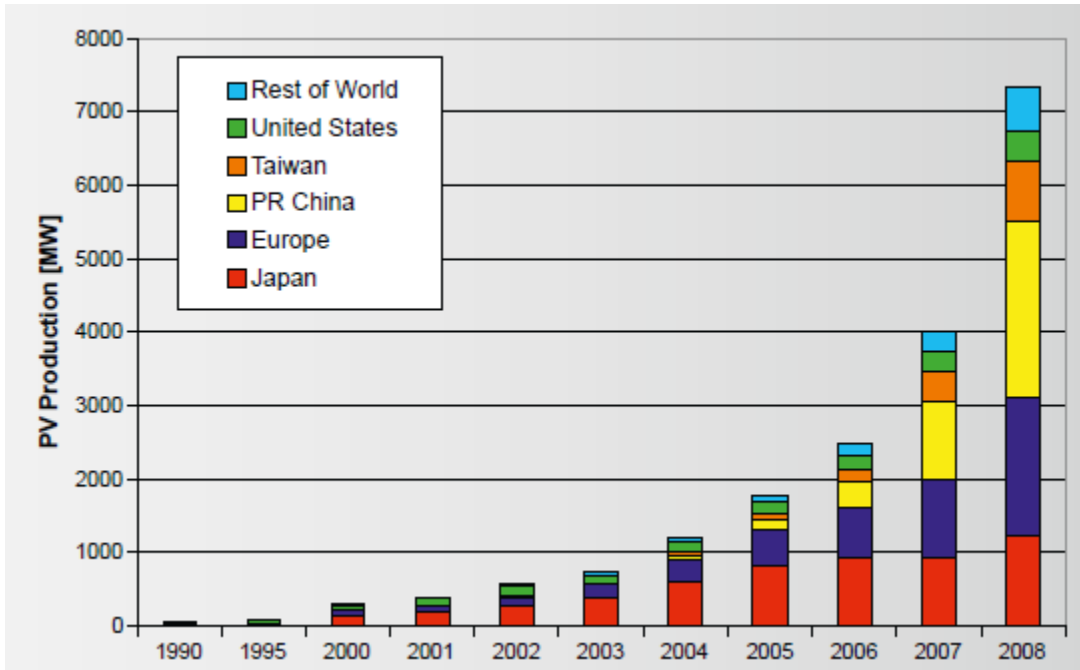


Figure 1.2 World photovoltaic production from 1990 to 2008 [4]

Covering 0.16 % of the earth's surface with 10 % efficient solar cells would produce 20TW of power [3]. In spite of having the potential to produce huge amounts of energy when used in a large scale, solar cells have not been able to replace fossil fuels as a primary source for commercial energy production because of the high costs involved in their production and deployment. To compete with fossil and nuclear energy the current cost per watt of grid solar power needs to be reduced by a factor of 50 [5]. To reduce the cost of photovoltaics and in a quest to find better performing materials, various

photovoltaic technologies have been investigated; they are classified into three generations based on the type of materials and junctions used.

The First generation of solar cells consists of single – junction silicon wafer based solar cells. Silicon wafer based solar cells exhibited high efficiencies, but involved high costs for the production of silicon wafers from quartzite and in running the processing machinery. Slicing the silicon ingot produced circular wafers which resulted in wastage of wafer area; and produced thicker wafers than were essential for solar cell manufacturing. Encapsulation for wafer cells too was expensive. Alternative forms of producing silicon for solar cells were investigated to avoid the huge costs involved in manufacturing silicon wafers. These produced multi-crystalline silicon with slightly lower performance. A process to produce ingots with a square cross-section was developed to make square silicon wafers instead of the circular wafers used conventionally. Other processes such as the edge-defined film-fed growth and the dendritic web process were developed to form sheets of silicon wafers directly to avoid the ingot method and the slicing steps it entails. First generation cells have achieved efficiencies of about 24% so far with around 3.5 \$/W cost, Figure 1.3, Figure 1.4. [6]

Thin film solar cells constitute the second generation of solar cells. Thin film based technologies such as Cadmium Telluride (CdTe), Copper Indium Gallium Selenide (CIGS), Gallium Arsenide (GaAs), amorphous silicon and semi-crystalline silicon overcome the huge costs involved in silicon wafer processing and can process larger unit areas (about 100 times) when compared to wafer-based technology [6]. The cost per watt for second generation solar cells varies from 3.5 – 0.5 \$/W and efficiencies of about 20% have been achieved so far, Figure 1.3, Figure 1.4.

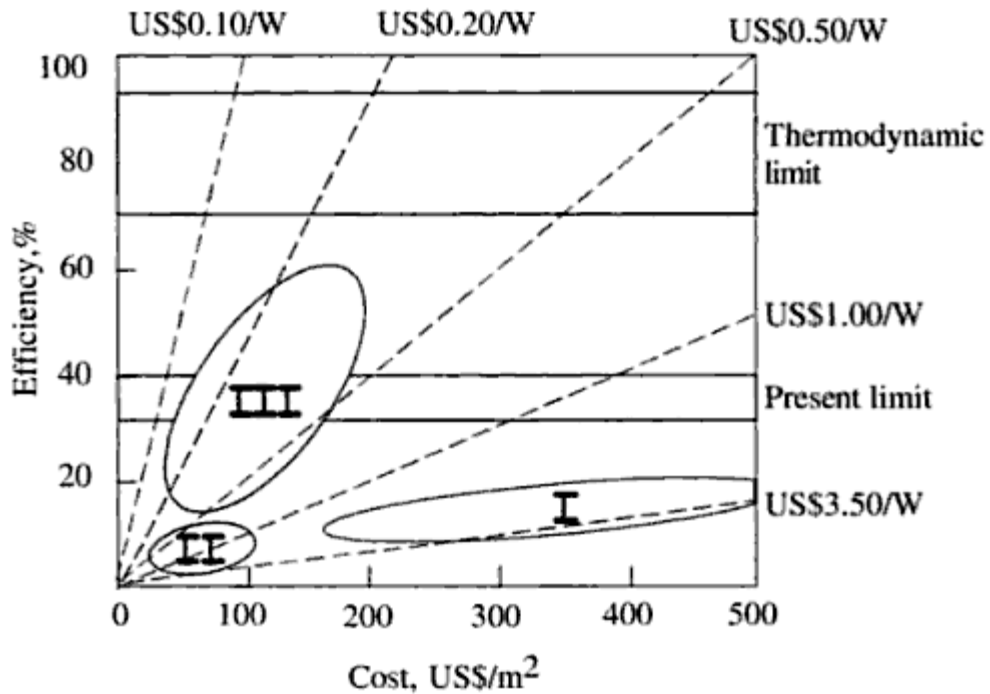


Figure 1.3 Efficiencies and costs for the three solar cell generations [7]

Third Generation photovoltaics encompass a wide range of emerging technologies to provide improved efficiencies and reduced costs compared to first and second generations. These cells use thin film deposition techniques like second generation cells and employ nontoxic materials. They target high efficiencies of the order of 20 – 60 % and thereby reduce the dollar per watt significantly to around 0.5 – 0.1 \$/W, Figure 1.3 [7]. Third generation photovoltaics consist of a wide range of cells: tandem or multi junction cells that have semiconductors of increasing band gap with the semiconductor of the highest band gap on top to enable collection of a wide range of solar spectrum; intermediate-level cells that have energy levels within the bandgap that contribute to photon absorption; multiple-electron hole pair cells that generated multiple electron –hole pairs per incident photon; hot carrier cells which are based on reduced

lattice interactions so that the carriers have the maximum time to get collected with high energies resulting in higher voltages at the output; die-sensitized cells and organic cells.

So far efficiencies of about 11.1% have been demonstrated, Figure 1.4 [7], [8], [9].

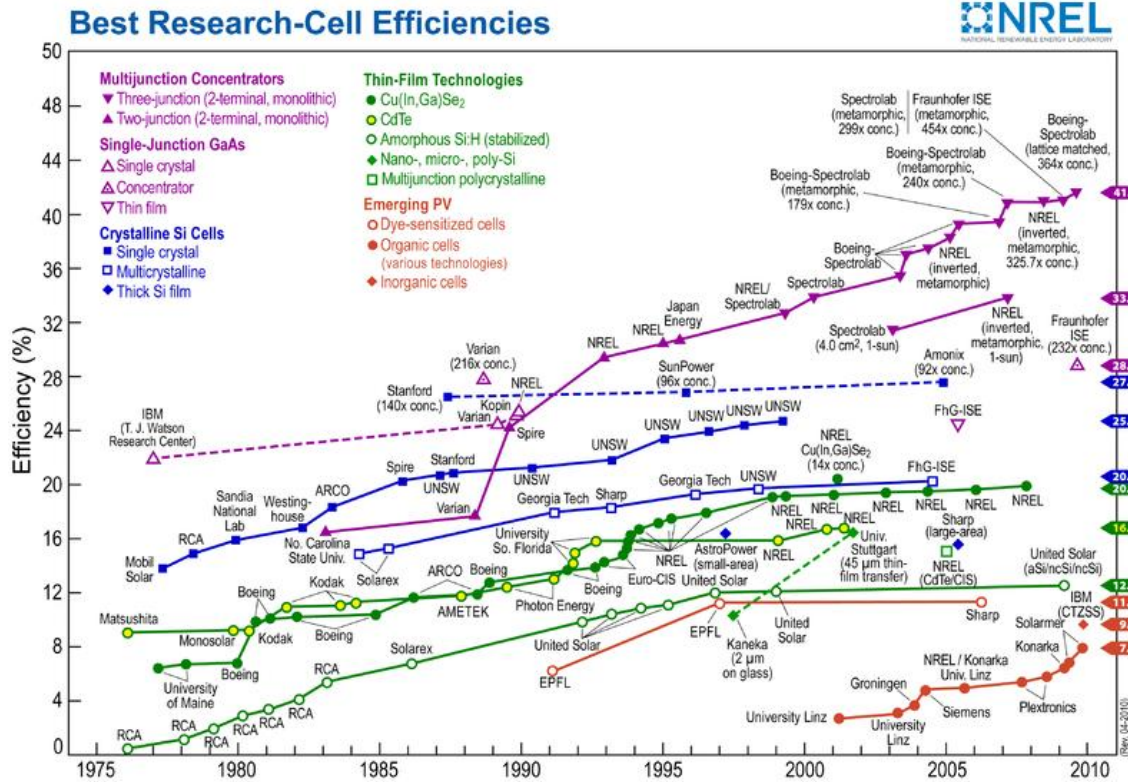


Figure 1.4 Best research-cell efficiencies [9]

Solar cells have an upper bound, called the thermodynamic limit, to the maximum efficiency they can achieve, Figure 1.3. This is because, when light is incident on a solar cell only the photons with energy greater than the band gap are absorbed, the rest are converted to heat. Moreover, even though all the absorbed photons generate electron-hole pairs only a part of them are collected at the output. More about this will be discussed in section III. The maximum theoretical efficiency that can be obtained by a single-junction solar cell is specified by the Shockley-Queisser limit to be 31 % under one sun conditions

and about 41% under 50,000 suns concentration; 50,000 suns indicates concentrating sunlight using lenses so that the intensity is equal to that of 50,000 suns [10]. Multiple junction cells capture a larger spectrum of the incident light and can reach higher efficiencies. Figure 1.5 lists theoretical efficiency limits for different solar cell configurations and the corresponding best efficiencies achieved so far. The table suggests that there is scope for improving the performance of existing cells and demonstrates the huge improvements in efficiencies that emerging technologies are capable of.

| <u>Approximate Theoretical Limit Efficiency</u> | | <u>Approximate Best Experimental Performance to Date</u> | |
|---|-----|--|---|
| Thermodynamic (concentrator) | 87% | n/a | |
| Thermodynamic (1 sun) | 68% | n/a | |
| Six-junction | 58% | n/a | |
| Hot carrier | 54% | n/a | |
| Triple-junction concentrator | 64% | 44% | III-V alloys, monolithic stack |
| Triple-junction (1 sun) | 49% | 15% | Thin-film amorphous silicon alloys |
| Double-junction concentrator | 56% | 30% | III-V alloys, monolithic stack |
| Double-junction (1 sun) | 43% | 12% | Thin-film amorphous silicon alloys |
| Shockley-Queisser single-junction (46,200 suns) | 41% | 30% | Crystalline silicon (500 suns) |
| Shockley-Queisser single-junction (1 sun) | 31% | 24% 20% 12% 6% | Crystalline silicon Thin multicrystalline silicon Dye-sensitized cell Organic cell |

Figure 1.5 Theoretical PV efficiency vs. experimental PV performance [10]

Solar Cell Operation

When light shines on a p-n junction, photons with energy greater than the band gap E_g of the semiconductor are absorbed. The following relation provides the conversion factor of wavelength to photon energy [11].

$$\lambda = \frac{c}{\nu} = \frac{1.24}{h\nu \text{ (eV)}} \mu\text{m} \quad (1.1)$$

Every material has an upper limit to wavelength, that corresponds to the band gap E_g beyond which it does not absorb photons.

When photons are absorbed by the semiconductor, photons of energy greater than the band gap E_g are absorbed and electron hole pairs are created throughout the device. Not all of these carriers are collected in the external circuit; only those carriers that are in the depletion region or within a diffusion length of the depletion region are collected, the rest are lost due to recombination, Figure 1.6.

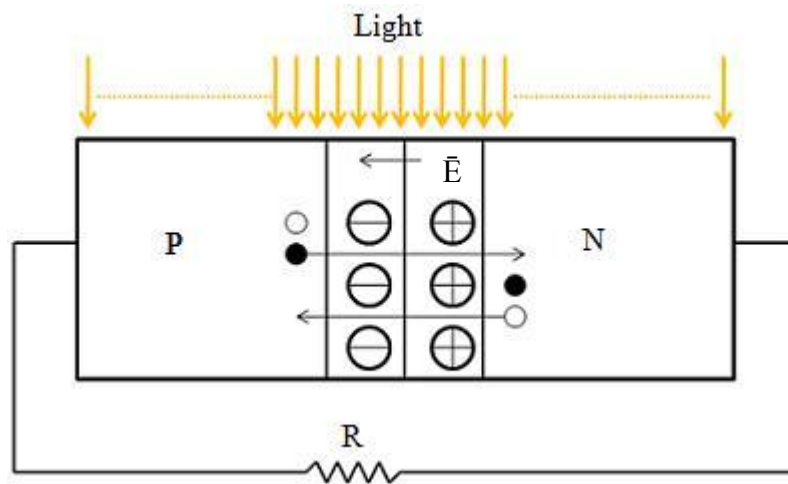


Figure 1.6 Working of a p-n junction solar cell

The following equation gives the ideal I–V characteristics of a solar cell

$$I = I_s(e^{qV/kT} - 1) - I_L \quad (1.2)$$

Where,

- I_s is the diode saturation current under reverse bias,
- I_L is the current due to excited carriers generated by solar radiation, Figure 1.7

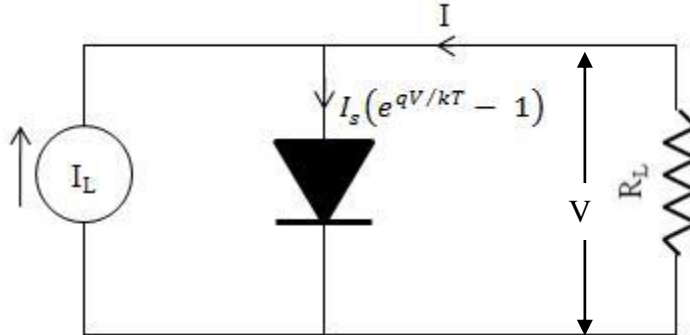


Figure 1.7 Equivalent circuit of an ideal solar cell [11]

I-V characteristics for an ideal solar cell are shown in Figure 1.8.

The open circuit voltage, V_{oc} and the short circuit current, I_{sc} are important parameters in evaluating the performance of a solar cell. V_{oc} is the voltage that appears across the terminals of a solar cell when they are not connected by a load. I_{sc} is the current that flows across a load of zero resistance. The voltage drop V across the load resistance R_L forward biases the diode and limits the total current across the load, the current I_L due to illumination is reduced by a factor of $I_s * (e^{qV/kT} - 1)$ (Figure 1.7), hence the maximum current obtained, I_m is always less than the short circuit current I_{sc} and the maximum voltage that can be collected, V_m is always less than the open circuit voltage V_{oc} .

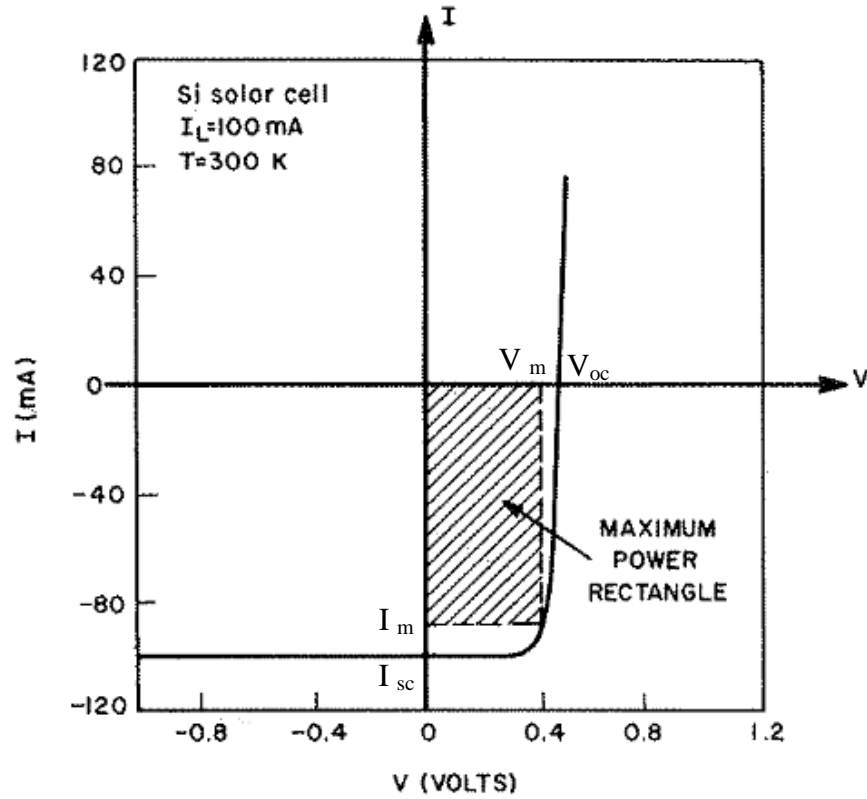


Figure 1.8 I-V characteristics of an ideal solar cell [11]

The efficiency for a solar cell is given by

$$\eta = \frac{V_{oc} * I_{sc} * FF}{E * A} \% \tag{1.3}$$

Where, The product ($V_{oc} * I_{sc} * FF$) is the maximum power generated by the solar cell in Watts,

E is the spectral irradiance in W/m^2 and

A is the surface area of the solar cell.

Solar Spectrum for Terrestrial Applications

The solar spectral irradiance curves in Figure 1.9 represent the solar spectra at various positions with respect to the earth. The air mass zero (AM0) condition represents the solar spectrum outside the earth's atmosphere and is considered for space applications. AM1 corresponds to the solar spectrum at the earth's surface when the sun is directly above or at its highest intensity with respect to that region of the earth's surface. Air mass 1.5 (AM1.5), that is sun at 45° above the horizon is considered a good average for terrestrial applications and the amount of solar power incident on the earth under these conditions is about 844 W/m^2 [11].

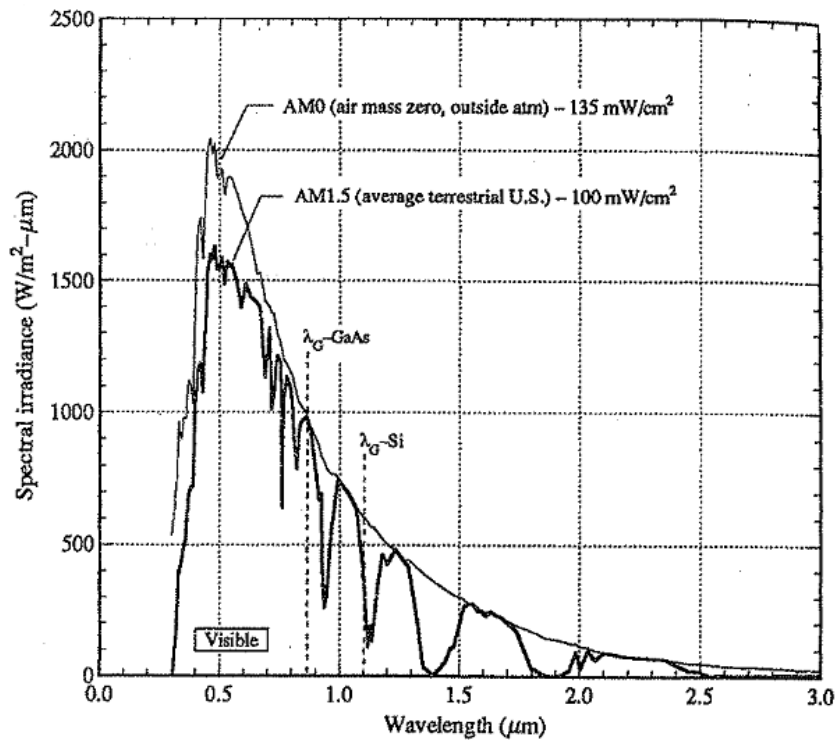


Figure 1.9 Solar spectra for AM 1.5, AM0 and 5800K black body [12].

Purpose and Content of This Thesis

The purpose of this Thesis was to investigate the effects of Molybdenum Nitride layers in the back contact structure of CdTe solar cells on cell performance.

The subsequent chapters are classified as follows: Chapter 2 discussed Metal – Semiconductor contacts in general, Chapter 3 discusses superstrate and substrate configuration solar cells, and Chapter 4 is a literature survey of back contacts to superstrate and substrate CdTe solar cells. Chapter 5 deals with the structure and properties of Molybdenum Nitride and Chapter 6 discusses characterization methods and experimental procedures involved in this study. Chapter 7 discusses the effects of Molybdenum Nitride in the back contact structure of CdTe solar cells to cell performance. Chapter 8 gives the conclusion from the current work and suggests future work that can be done to further support the explanation given here. Also suggestions for further improvement of CdTe solar cells based on Molybdenum Nitride back contacts are made.

CHAPTER 2:

METAL SEMICONDUCTOR CONTACTS

The Schottky – Mott Theory

Formation of reliable and stable ohmic contacts to semiconductors is very important to ensure efficient current collection. Contacts to semiconductors can either be rectifying or ohmic depending on the characteristics of the metal. Metal –Semiconductor contacts as explained by the Schottky-Mott Theory will be discussed in this section. The Schottky-Mott theory is based on a few assumptions; (1) There is no intermediate layer between the metal and the semi-conductor such as an insulating layer of oxide. (2) No change in the metal – semiconductor boundary after contact (3) No surface charges. [13], [14]

The semiconductor work function, Φ_S is given by the sum of the semiconductor electron affinity, χ_s and the energy difference between the conduction band of the semiconductor, E_C and the semiconductor Fermi level, E_F [12], [15].

$$\Phi_S = \chi_s + (E_C - E_F) \quad (2.1)$$

The electron affinity of the semiconductor χ_s which is the energy difference between the vacuum level and the conduction band of the semiconductor ($\chi_s = E_0 - E_F$) is constant for a given semiconductor and $(E_C - E_F)$ decreases with increasing doping density in the semiconductor. The work function Φ_M is constant for a given metal [12], [15].

Contacts to an N-type Semiconductor

N-type semiconductors form ohmic contacts when contacted with metals of work function lower than that of the semiconductor ($\Phi_M < \Phi_S$) and rectifying contacts to metals of work function higher than the semiconductor work function ($\Phi_M > \Phi_S$). The barrier height for an N-type semiconductor in contact with a metal is given by

$$\Phi_B = \Phi_M - \chi_s \quad (2.2)$$

Figure 2.1 shows the band diagrams before and after contact of a metal and an n-type semiconductor

Contacts to a P-type Semiconductor

P-type semiconductors form rectifying contacts to metals of work function lower than that of the semiconductor ($\Phi_M < \Phi_S$) with the barrier height given by

$$\Phi_B = E_G + \chi_s - \Phi_M \quad (2.3)$$

and ohmic contacts to metals of work function higher than the semiconductor work function ($\Phi_M > \Phi_S$) [12], [15]. Figure 2.2 shows the band diagrams before and after contact of a metal and a p-type semiconductor.

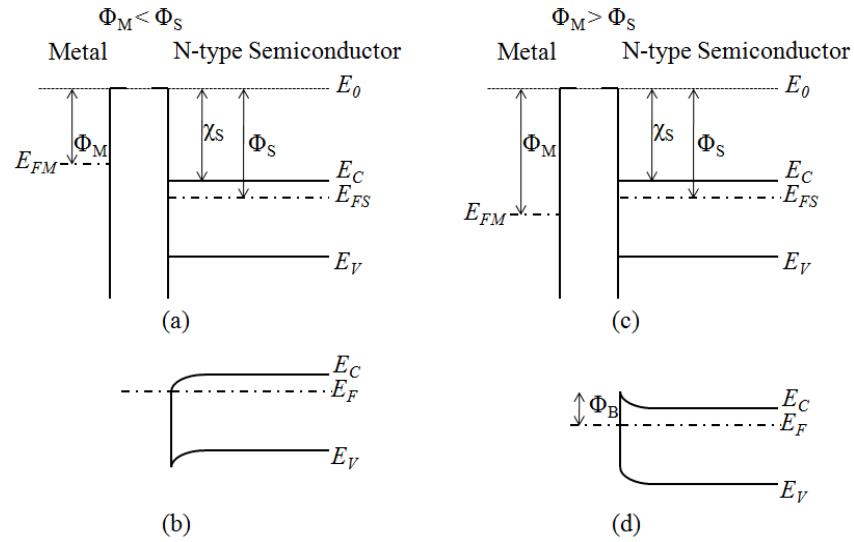


Figure 2.1 Energy band diagrams of metal and N-type semiconductor contacts when (1) The metal work function is less than the semiconductor work function, ($\Phi_M < \Phi_S$) (a) before contact and (b) after contact, ohmic or accumulation type contact. (2) The metal work function is greater than the semiconductor work function, ($\Phi_M > \Phi_S$) (a) before contact and (b) after contact, rectifying or depleting type contact. [12], [15]

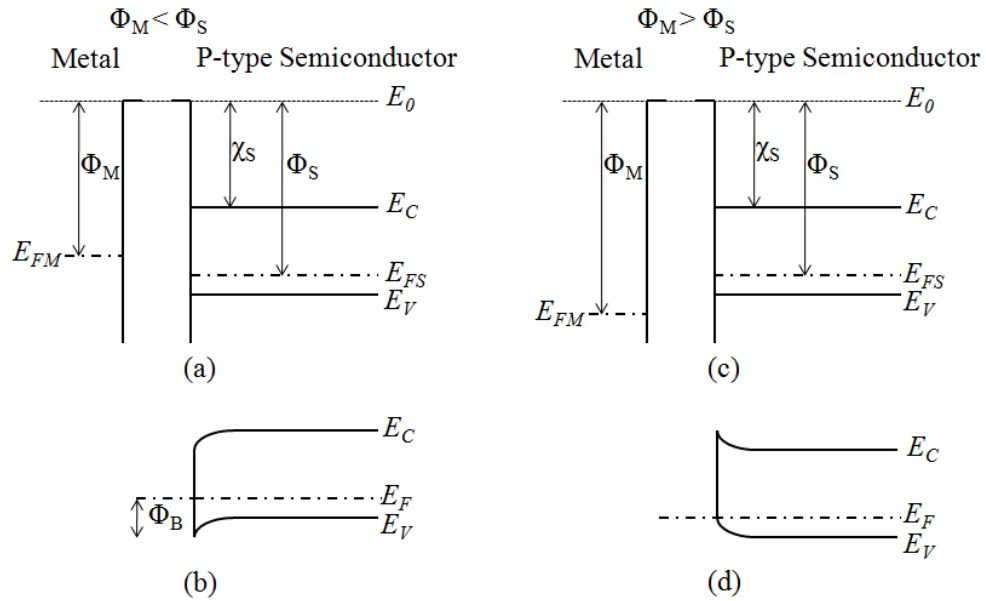


Figure 2.2 Energy band diagrams of metal and P-type semiconductor contacts when (1) The metal work function is less than the semiconductor work function, ($\Phi_M < \Phi_S$) (a) before contact and (b) after contact, rectifying or depletion type contact. (2) The metal work function is greater than the semiconductor work function, ($\Phi_M > \Phi_S$) (a) before contact and (b) after contact, ohmic or rectifying type contact. [12], [15]

The Bardeen Model

According to the Schottky-Mott Theory, ohmic contacts can be formed by choosing the metal with the appropriate work function. But, it has been found experimentally that the Schottky barrier height is less sensitive or even independent of the metal work function in some cases [16], [14], [13]. John Bardeen attributed this to surface states on the semi-conductor surface and explained the weak dependence of the barrier height to the metal work function [14].

Surface states exist on the free surface of a semiconductor because the periodic structure of the crystal lattice is terminated at the surface. These surface states have energies inside the band gap for some semiconductors which causes the Fermi level to be pinned. A double layer or dipole is formed that consists of electrons in surface states and a space charge in the semiconductor of opposite sign due to transfer of electrons from the region in the bulk immediate to the surface into surface states. When the density of surface states is very high ($>10^{13} \text{ cm}^{-3}$), the work function at the free surface of a semiconductor is determined entirely by the surface and is independent of the Fermi level in the semiconductor. This semiconductor when contacted to a metal gives a potential rise in the semiconductor that is equal to that on the free semiconductor surface and the amount by which the potential is raised at the semiconductor surface is practically independent of the metal work function. [14], [13], [17]

Ohmic Metal-Semiconductor Contacts

Ohmic or pseudo-ohmic metal-semiconductor contacts can be formed by (1) Heavily doping the semi-conductor adjacent to the metal (2) Using an interface layer with a work-function suitable to the semiconductor that ensures a low barrier height (3) Adding recombination centers to the semiconductor adjacent to the contact (4) Changing the Fermi level pinning at the metal-semiconductor interface. [18]

Doping the Semiconductor

The current flow between a lightly doped semiconductor and a metal is by thermionic emission. This is illustrated in Figure 2.3 for a metal and an n-type semiconductor. In this mechanism of current flow, the majority carriers, which are

electrons in this case, need to be thermally excited over the barrier. Not many electrons have sufficient energy to overcome this barrier at low kT values and conduction is minimal. Doping the semiconductor adjacent to the metal to high concentrations results in a very narrow depletion width and carriers can tunnel through the barrier. This mechanism known as field emission is the dominant mechanism for low kT values or for normal operation conditions. [15]

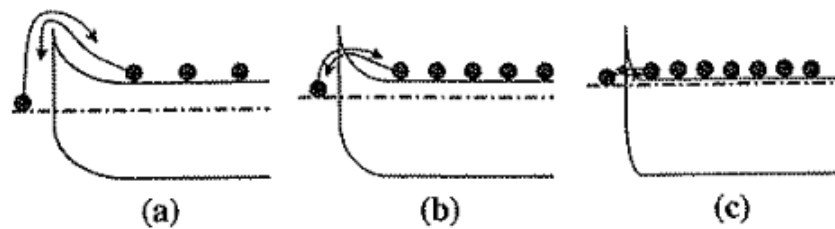


Figure 2.3 Carrier flow based on increasing dopant concentration for a depleting n-type metal-semiconductor contact: (a) Thermionic emission for low doping concentrations (b) Thermionic and Field emission for moderate doping concentrations (c) Field emission for high doping concentrations [15]

Intermediate Layers

As explained by the Schottky-Mott theory in section I, to form ohmic contacts, n-type semiconductors need to be contacted to low work function metals and p-type semiconductors should be contacted to high work function metals. There exist many low work function metals, but metals with high enough work functions to make ohmic contacts to some semiconductors and compound semiconductors like CdTe do not exist. In such cases an intermediate layer of high work function can be employed between the semiconductor and the metal to form a non-rectifying contact.

An intermediate layer can also be a layer that can be doped to higher doping concentrations when compared to the actual semiconductor which is to be contacted, like ZnTe which can be doped to high acceptor concentrations when compared to p-type CdTe [18].

Adding Recombination Centers

Ohmic contacts are defined as regions with high carrier recombination rates. Semiconductor regions that are highly damaged will have high recombination rates in the form of multistep tunneling. In order to generate high recombination centers, the junction is hit by a short, intense electrical discharge. Though this process generates defects and recombination in the form of multistep tunneling, it also lowers the carrier density. But damaging semiconductors this way is not desirable because of the random nature and irreproducibility involved in the process. Moreover, this approach does not work for the material of interest here i.e CdTe. [15], [18]

Modifying the Fermi Level Pinning at the Metal-Semiconductor Interface

As explained in section II, the schottky barrier height is independent of the work function in many cases because of Fermi level pinning. The Fermi level tends to be pinned because of a high density of surface states ($>10^{13} \text{ cm}^{-3}$) as discussed in Chapter 2, section II, Modifying the Fermi level pinning at the metal-semiconductor interface can help achieve ohmic contacts [18]. Various surface treatment methods have been investigated to modify the CdTe surface such as cleaving, mechanical polishing, chemical etching and sputter etching [19].

CHAPTER 3:

THIN FILM CADMIUM TELLURIDE SOLAR CELLS

Cadmium Telluride Solar Cells

Cadmium Telluride with a direct band gap of 1.45 eV and a high absorption coefficient greater than 10^5 cm^{-1} is very suitable for solar absorption. Cadmium Telluride (CdTe) solar cells being economical have the potential for commercial production. CdTe is inherently p-type at sufficiently high temperatures and this makes it easier to use in solar cells [20]. These cells have been predicted to reach efficiencies of the order of 30% under one sun and about 35% under 1000 suns condition for terrestrial applications, Figure 3.1 [21].

Solar cells with CdTe as the absorber and CdS as the window layer have been conventionally fabricated on glass and are referred to as the superstrate configuration solar cells.

Superstrate CdTe Solar Cells

A basic superstrate CdTe solar cell configuration is shown in Figure 3.2. It consists of a transparent conducting oxide, such as (Indium Tin Oxide) ITO deposited on glass and an n-type CdS layer deposited on top of the TCO layer. The CdS layer reduces the surface recombination rate of carriers and having a band gap of 2.42 eV acts as a window for photons that are absorbed in the CdTe absorber with a band gap of 1.45 eV.

P-type CdTe is deposited on top of the CdS layer and is treated with CdCl₂ annealing for activating the cells [20]. CdCl₂ treatment enhances grain growth, reduces interface state density and causes an increased CdS diffusion into CdTe resulting in improved an response in the UV region [22]. This is usually followed by a Br: CH₃OH etch or a NP(Nitrogen Phosphorus) etch which makes the CdTe surface Tellurium (Te) rich resulting in high hole densities hence forming a good ohmic contact to metals [23]. A metal like molybdenum that can withstand high temperatures (Molybdenum has a melting point of 2623°C) and is chemically stable is deposited for current collection across an external load.

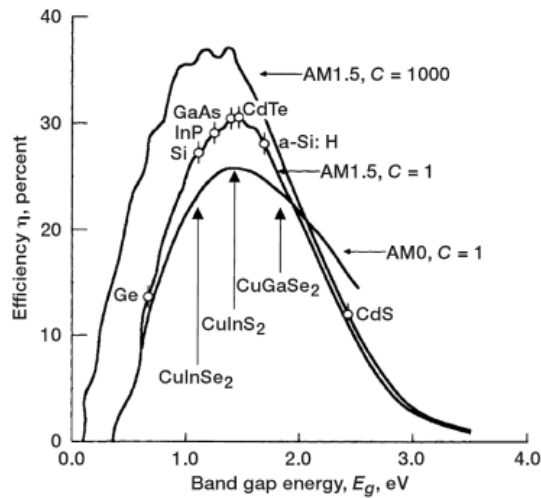


Figure 3.1 Predicted efficiency versus band gap for thin film solar cells [21]

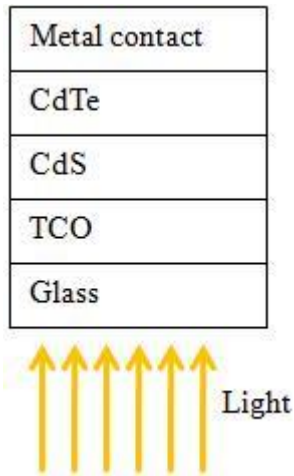


Figure 3.2 Basic superstrate CdTe solar cell configuration

Substrate CdTe Solar Cells on Flexible Substrates

CdTe solar cells have been made on flexible polymer substrates both in substrate (polymer/Back contact/Interface Layer/CdTe/CdS/ITO) and superstrate configuration (polymer/ITO/CdS/CdTe/Interface Layer/Back contact) [24]. CdTe solar cells on metallic flexible substrates like molybdenum and stainless steel foil too have been developed.

The present work focuses on CdTe solar cells on stainless steel foil substrates. Stainless steel not being transparent (unlike glass), the metal contact is deposited first. An interlayer may be deposited followed by p-type CdTe / n-type CdS. This is followed by CdCl₂ treatment and ITO sputtering for the front contact. A typical substrate CdTe solar cell on stainless steel substrates is shown in Figure 3.3. This configuration of CdTe solar cells on metallic substrates is referred to as the substrate configuration. Substrate CdTe solar cells involve flipping the layers in the superstrate cell which entails many challenges, not encountered in superstrate cells.

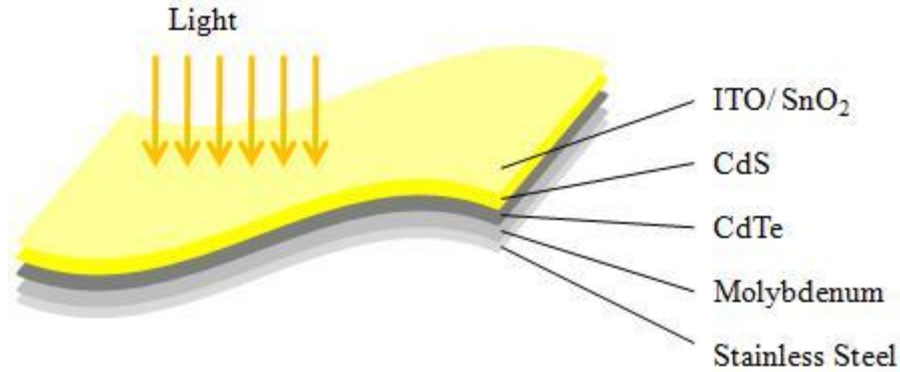


Figure 3.3 Basic substrate CdTe solar cell structure

Challenges in Substrate CdTe Solar Cells

Even though the record efficiency for superstrate CdTe cells is 16.7 %, the reported record for substrate solar cells on flexible metal foil substrates is only 7.8 % [25]. A major reason for lower efficiency for substrate CdTe solar cells is the poor back contact [24]. Substrate CdTe Flexible substrates also have a disadvantage of having a narrower choice of materials when compared to superstrate solar cells; because they require materials with matching thermal expansion coefficients. It is also difficult to get a uniform completely covered CdS film on top of the rough CdTe surface in the case of substrate cells [24].

Some drawbacks with back contacts in substrate cells which are not present in superstrate cells are (1) The absence of a tellurium rich layer formed by Br: CH₃OH etch that helps in the formation of a good ohmic contact. (2) The back contact to CdTe is affected by subsequent CdCl₂ treatment [24]. (3) The deposition of subsequent layers involves high temperatures causing impurity diffusion out of the stainless steel substrate.

CHAPTER 4:

BACK CONTACTS TO CADMIUM TELLURIDE SOLAR CELLS

History of Back Contacts to Cadmium Telluride Solar Cells

Cadmium Telluride (CdTe) has a high electron affinity of 4.5eV and a band gap of 1.5eV, resulting in a high work function for p-type CdTe [26]. Because of the lack of metals with work functions high enough to form ohmic contacts to p-type CdTe, contacts to p-type CdTe are rectifying. Moreover, the presence of a high density of surface states on CdTe might cause the metal/CdTe interface to be pinned resulting in a non-rectifying contact even with a high work function metal [19], [26], [14]. It is hence necessary to modify the CdTe region or surface before contacting it to a metal. The CdTe surface is typically etched with a NP (HNO_3 , H_3PO_4), $\text{K}_2\text{Cr}_2\text{O}_7 + \text{H}_2\text{SO}_4$ or $\text{Br}_2/\text{CH}_3\text{OH}$ to form a p+ Tellurium rich surface. A number of different approaches with various materials have been investigated to achieve ohmic contacts to p-type cadmium telluride for CdTe solar cells.

Metal Contacts to P-type CdTe

Various metals have been deposited directly on etched p-type CdTe as contacts to CdTe solar cells. Metals with high work functions or metals that can be used as acceptors to dope CdTe p+ are typically used. Conventional back contacts to CdTe employ Cu/Mo

[27], Cu/Au [28], [29] or Cu/graphite [30]. Chou et al. studied Au/Cu contacts to CdTe solar cells and have observed Cu diffusion into CdTe and substitutional acceptor doping of Cd sites [31]. Degradation of cell performance was observed when excess Cu was used; due to the diffusion of Cu through CdTe and formation of recombination centers and shunt paths [31]. To overcome the degradation of cell performance due to Cu diffusion to the CdTe/CdS junction, Sb/Au has been employed as a back contact [32]. Ni-P contacts with subsequent annealing causing P diffusion into CdTe have been employed to form a p⁺ region between the metal and CdTe; a contact resistivity of 0.1-0.08 Ωcm^2 was achieved [33]. Ni₂P mixed with graphite paste was used as a back contact, and it was observed that annealing leaves the CdTe bulk essentially unaffected modifying only the surface in contact with the metal. Ni₂P has hence been shown to be stable unlike Cu which diffuses over time [34].

P⁺ Doping of CdTe

CdTe can form ohmic contacts to metals by directly doping the CdTe region highly p⁺. The carrier density and conductivity in CdTe depends to a large extent on defects in CdTe. CdTe can be n-type or p-type depending on the type of vacancies or defects present. CdTe is p-type at low cadmium pressures due to excess tellurium that results in Cd vacancies and Te interstitials; and is n-type at high cadmium pressures due to excess cadmium because of Te vacancies and Cd interstitials. This behavior has also been observed for CdTe with Cu and Au impurities. [23]

CdTe being a II-VI compound, can be doped with acceptor impurities of group I and V. Single-crystal p-type CdTe can be easily doped to acceptor levels greater than

10^{17} cm^{-3} with P, V, Li, Na. [35], [36], [37], [38], [39], [40], [36] but the maximum achievable acceptor doping in CdTe is limited due to self-compensation [41]. Thin film deposition processes used for manufacturing CdTe solar cells result in the formation of polycrystalline films which are more difficult to dope, moreover the resistivity for polycrystalline material is higher compared to single crystal material due to grain boundary or surface scattering effects. [42].

Chu et al. have tried varying the acceptor density of CdTe by changing the Te/Cd ratio and by doping p-type CdTe with Arsenic, Phosphorus or Oxygen; they have been able to achieve acceptor concentrations in the range of $0.2 \times 10^{16} \text{ cm}^{-3} - 1 \times 10^{16} \text{ cm}^{-3}$ [43]. H. Zhao et al. have been able to introduce antimony and oxygen impurities to about 10^{16} cm^{-3} [44].

Interlayers between CdTe and the Metal Contact

Because of the difficulties involved in doping polycrystalline CdTe to high acceptor concentrations and because of the lack of availability of metals with high enough work functions to form ohmic contacts to p-type CdTe (which has a work function of around 5.9 eV), interlayers are used to form good ohmic contacts between metal and p-type CdTe.

HgTe and HgCdTe have been used as buffer layers for CdTe solar cells. HgTe is a semi-metal and has a work function of 5.9 eV close to that of CdTe (5.9 - 6 eV). [45], [46]

M. Florez et al utilized a Cu_2Te interlayer to reduce the amount of Cu segregation at the CdS/CdTe interface due to diffusion and were able to form low resistance contacts with contact resistivity of $0.16 \Omega\text{cm}^2$ to CdTe with the help of a Cu_xTe interlayer formed by etching the CdTe films in Sulphochromic (100ml, 20% $\text{K}_2\text{Cr}_2\text{O}_7$ + 50 ml conc. H_2SO_4) followed by dipping in CuCl_2 and then contacting with Cu [47]. J. H. Yun et al. deposited a Cu_2Te layer directly on CdTe and were able to achieve a minimum series resistance of $0.5 \Omega\text{cm}^2$ due to formation of hexagonal phases of Cu_2Te by annealing above 200°C forming a good lattice match to CdTe [48].

Stable CdTe solar cells with Sb and Sb_2Te_3 interlayers and molybdenum metallization have been used to substitute Cu containing back contacts which degrade solar cell performance over time due to the diffusion of Cu causing the cell to be shorted [49].

Conductivity from CdTe to the back contact is through holes and it is necessary to form a minimum barrier to the flow of holes, by achieving a zero valance band offset [50], [51], [52]. Contacting CdTe to metals directly forms large schottky barriers, obstructing the flow of holes. ZnTe serves a dual purpose in that it can be doped with Sb doping of up to 10^{18}cm^{-3} facilitating tunneling when contacted to a metal and achieving a very small valence band offset of 0.05 eV with CdTe. [50], [51], [52]

T. Tang et al. studied Cu-doped ZnTe films as an intermediate layer between CdTe and the metal contact. CdTe is difficult to dope to high acceptor concentrations. ZnTe has a small valence band discontinuity with CdTe and can be doped degenerately with Cu. ZnTe doped with Cu has been used with Au, Ni and Co as metal contacts. It has

been observed that introduction of the ZnTe layer significantly reduced the series resistance of the CdTe/CdS solar cells from 1.8 to 0.1 Ωcm^2 [53]. T. A. Gessert et al manufactured solar cells with ZnTe: Cu / Ti back contacts [54].

History of Back Contacts to Substrate Cadmium Telluride Solar Cells

As mentioned in Chapter 3, back contacts to CdTe solar cells on metallic substrates in the substrate configuration face various challenges not encountered by superstrate cells. Back contacts that have been used conventionally for superstrate solar cells cannot be employed as back contacts to substrate cells because of mismatch in the thermal expansion coefficients to CdTe and/or the metallic substrate or degradation of the back contact caused by CdCl₂ annealing. CdTe solar cells have been developed in the substrate configuration on polymer foil with efficiencies of 7.3% [24]. V. P. Singh et al have tried using HgTe and ZnTe as interlayers but without much success [55]. Molybdenum was employed as the back contact followed by a Cu/Te interlayer on Molybdenum substrates and it was observed that CdCl₂ annealing and O₂ annealing improved cell V_{oc} ; a highest cell efficiency of 5.3% was reported [55]. Matulionis et al. have been able to achieve efficiencies of 7.8% with N₂ doped ZnTe as an interlayer between molybdenum and CdTe [25]. Enrique et al employed Mo back contacts with Au/Pd as an interlayer on molybdenum substrates because of the matching thermal expansion coefficient of molybdenum ($4.8 \times 10^{-6}/\text{K}$) with CdTe ($5 \times 10^{-6}/\text{K}$) and have achieved efficiencies of 3.5% [56].

CHAPTER 5:

MOLYBDENUM NITRIDE

Transition Metal Nitrides

Transition metal nitrides exhibit high hardness, high melting points and good chemical and physical stability and have been used as surface coatings, catalysts and high temperature ceramics. Nitrides of the d-block transition metals are close-packed compounds. Nitrogen having a much smaller atomic size compared to transition metals, occupies the octahedral interstitial sites between the metal atoms of transition metal nitrides [57], [58]. Most binary transition metal nitrides exist in the cubic NaCl structure and the hexagonal WC structure [57].

Crystal Structure of Molybdenum Nitride

The phase diagram of the Molybdenum – Nitrogen (Mo –N) system is shown in Figure 5.1. The Mo –N system exists in the following phases

(i) α phase: In this phase Molybdenum (Mo) has very little nitrogen from 0 to 1.08 at. %. Molybdenum exists in the body centered cubic lattice system in α phase. The nitrogen atomic concentration in α -Mo is very low below 1000°C and reaches the maximum concentration of 1.08 at. % at the eutectic temperature of 1860°C where the solidus and liquidus lines intersect. [59]

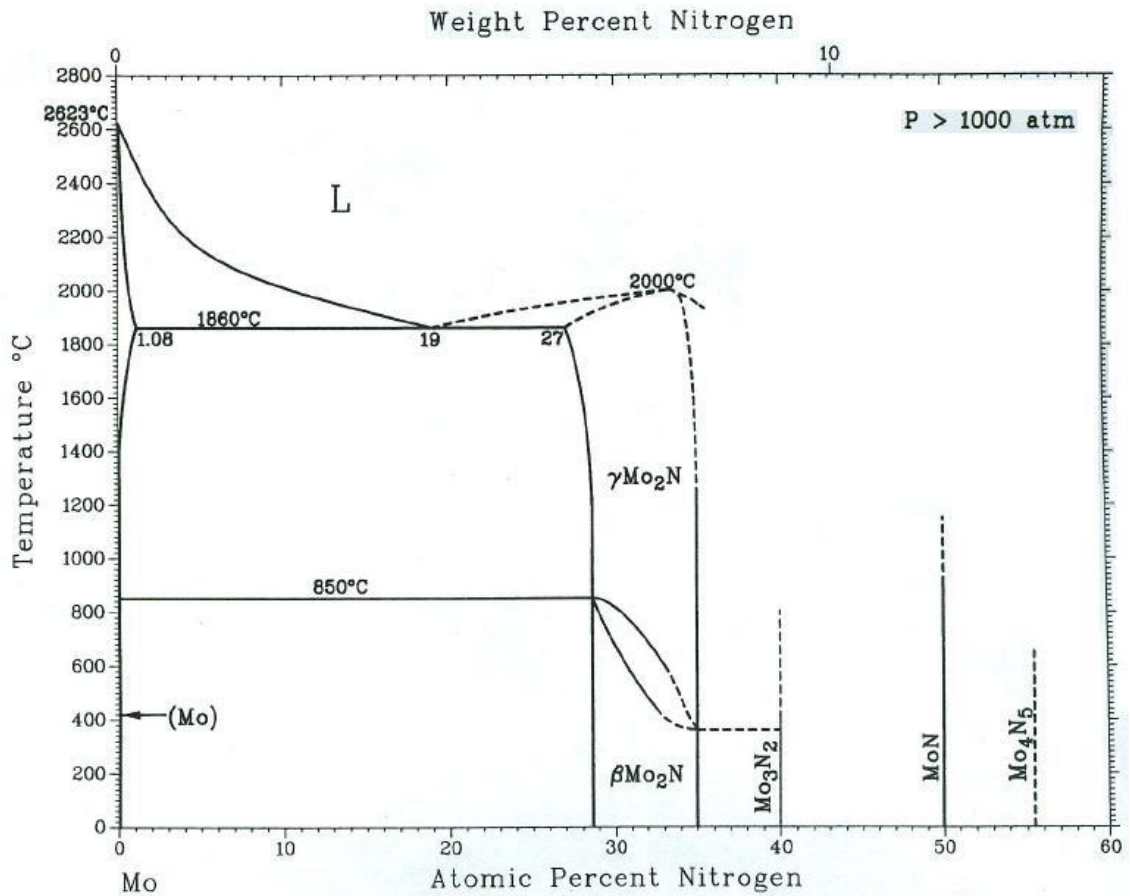


Figure 5.1 Molybdenum – nitrogen phase diagram [60]

(ii) β phase: Molybdenum and nitrogen crystallize at low temperatures to form β - Mo_2N . β - Mo_2N crystals are face centered tetragonal with an ordered array of nitrogen atoms and nitrogen concentrations of 28.7 to 35 at.%. The lattice constants for the β - Mo_2N unit cell are $a = b \neq c$. β - Mo_2N has a $I4_1/amd$ structure as shown in Figure 5.2 and is considered “a tetragonal modification of the cubic γ - Mo_2N phase” with the lattice constant ‘c’ doubled [61], [59], [62], [63].

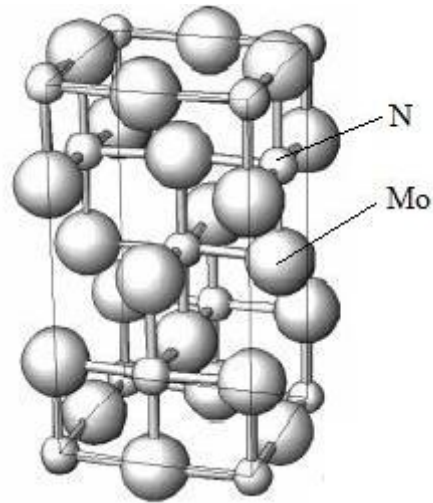


Figure 5.2 Crystal structure of β - Mo_2N [64]

(iii) γ phase: γ - Mo_2N contains nitrogen atomic concentrations of 27 – 35 at. % and is formed at high temperatures as a face-centered cubic lattice with a defective B1 structure (Figure 5.3), with half of the nitrogen sublattice positions vacant [65], [61]. There also exists a B1-MoN phase, which is formed by increasing the nitrogen concentration and by filling up the vacant sites in the nitrogen atom sublattice in the defective B1 γ - Mo_2N structure [66]. But the B1-MoN is not shown in the phase diagram because it is thermodynamically unstable and the thermodynamically stable hexagonal δ -MoN is formed instead [66], [67].

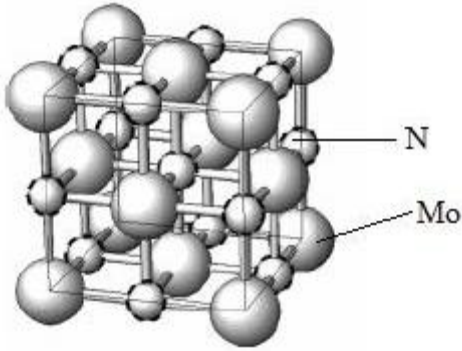


Figure 5.3 Crystal structure of γ Mo₂N [64]

(4) δ phase: δ -MoN is formed at 50 at. % nitrogen and has a hexagonal structure and belongs to the P6₃mmc space group, Figure 5.4. [59]. Some weak extra lines in the X-ray diffraction pattern indicate the presence of a superlattice [68].

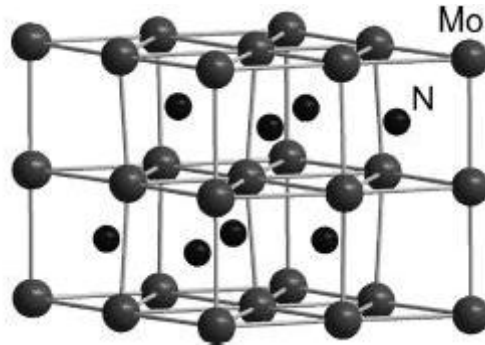


Figure 5.4 Crystal structure of δ -MoN [69]

Structural and Mechanical Properties of Molybdenum Nitride

Sputtering of Molybdenum targets in the presence of Ar and N₂ gases, leads to the formation of γ -Mo₂N for lower nitrogen concentrations and hexagonal δ -MoN at higher nitrogen concentrations [66], [70]. Properties of Mo-N films and the variation of these properties with the phase of Mo-N will be explained.

The hardness of molybdenum nitride films, MoN_y changes with the nitrogen stoichiometry 'y' and with the phase of Mo-N. The hardness of molybdenum nitride films decreases with increasing 'y' in the presence of fcc $\gamma\text{-Mo}_2\text{N}$ [70]. This trend in hardness is related to the strength of the Mo-N bond. Initially, for low nitrogen concentrations, electrons in the low-lying bonding bands corresponding to the 4d sublevel in Mo (with electron configuration $[\text{Kr}] 5s^1 4d^5$) and the 2p sublevel in N (with electron configuration $1s^2 2s^2 2p^3$) hybridize strongly to form a Mo-N covalent bond, resulting in high hardness. With increasing nitrogen concentration, the low-lying bonding bands are all occupied by electrons and the additional electrons occupy the higher-lying antibonding bands. This causes the covalent bond to be broken creating a weaker ionic bond; hence the hardness decreases. [67] With the appearance of the hexagonal $\delta\text{-MoN}$ the hardness increases because of a higher cohesive energy.

The $\delta\text{-MoN}$ phase has a higher bulk modulus compared to $\gamma\text{-Mo}_2\text{N}$. E. Soignard et al. have reported a bulk modulus of 345 GPa for $\delta\text{-MoN}$ and 301 GPa for $\gamma\text{-Mo}_2\text{N}$ [71]. The higher bulk modulus in the case of $\delta\text{-MoN}$ is in turn due to the higher cohesive energy for $\delta\text{-MoN}$.

Higher hardness is generally observed in films with high compressive stress where as softer materials exhibit tensile stress. P. Hones et al. have determined the residual stress in Mo-N films and have found that $\gamma\text{-MoN}$ films exhibit tensile stress with 1.6 ± 0.4 GPa, B1 $\text{MoN}_{0.8}$ films show a tensile stress of 2.05 ± 0.1 GPa and $\delta\text{-MoN}$ films show a compressive stress of -3.3 ± 0.2 GPa. [70]

The δ -MoN films are densely packed and highly ordered films and stable compared to the other phases of Mo-N [70], [71], [72].

CHAPTER 6:

CHARACTERIZATION METHODS AND EXPERIMENTAL PROCEDURE

Four-point Probe

The four-point probe measurement technique was used to determine the resistivity of the thin films investigated in this work.

The experimental setup for the four-point probe is shown in Figure 6.1. A DC voltage is applied between probes 1 and 4 and the ammeter connected between probes 1 and 4 measures the current 'I' across the device. Due to the voltage drop across wire resistances R_{w1} and R_{w4} , the four-point probe uses a different set of probes to measure current and voltage. The high impedance of the voltmeter ensures negligible current flow across wire resistances R_{w2} and R_{w3} and hence an accurate voltage 'V' is recorded [15].

The four-point probe by Signatone Corporation employed in this case had probes equally spaced at 1mm. A DC voltage of 1V was applied between probes 1, 4 using a '6825A Bipolar Power Supply / Amplifier by Hewlett Packard' set to a range of 2.4V and the current I and voltage V were measured using two '8010A Digital Multimeters by Fluke' across probes 1, 4 and 2, 3 respectively. The multimeters for measuring current and voltage were set to read a maximum current of 20mA and a maximum voltage of 200mV respectively. The films measured using the four-point probe, were less than 1 μ m

thick. For probes that are equally spaced at a distance s , and for a film thickness $t \leq s/2$, which is true in our case, the sheet resistance is given by [15]

$$R_s = 4.532 \frac{V}{I} \quad (6.1)$$

Hence the sheet resistance R_s was calculated from the voltage ‘V’ and ‘I’ that were measured. The thickness t of the films was measured using a ‘Veeco-DekTak 6M Surface Profiler’. The resistivity ρ of Molybdenum (Mo) and Molybdenum Nitride (Mo-N) deposited were obtained by using the following relation,

$$\rho = R_s * t \quad (6.2)$$

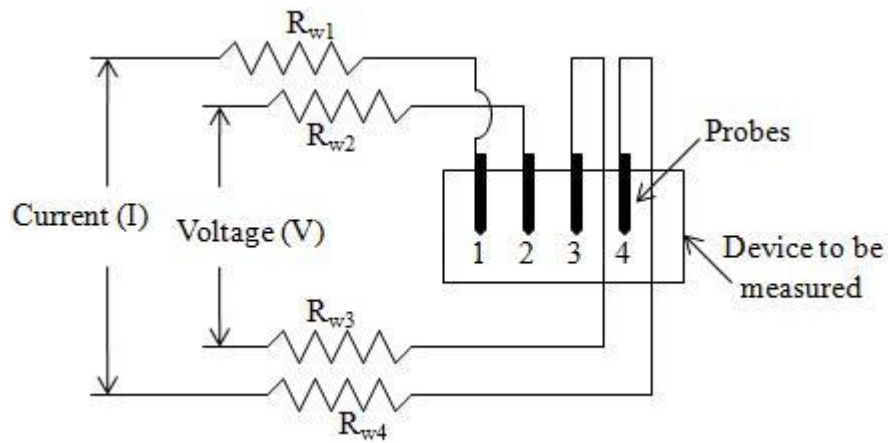


Figure 6.1 Four-point probe [15]

X-Ray Diffraction Spectroscopy (XRD)

X-rays are electromagnetic radiation with short wavelengths in the range of 0.01 – 10 nm comparable to atomic spacing. X-ray Diffraction is a non-destructive technique for determining the chemical composition, crystallographic structure and physical properties

of materials and thin films. The properties of the material or thin film are determined by the X-rays that are diffracted by the crystal lattice.

When X-rays with wavelength λ are incident at an angle θ onto a crystalline solid with crystal planes spaced at a distance d , these X-rays are scattered by the crystal lattice and X-rays that constructively interfere are recorded by an X-ray detector [73]. The path difference between rays diffracted constructively from adjacent crystal planes is $2d\sin\theta$, as shown in Figure 6.5. The condition for constructive interference as given by Bragg is

$$2d\sin\theta = n\lambda \quad (6.3)$$

Where n is an integer.

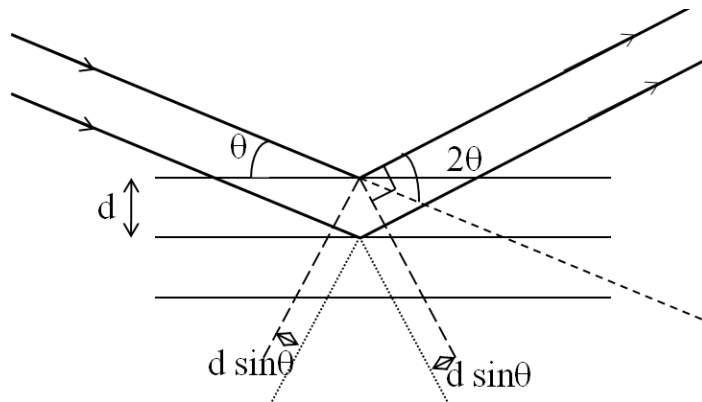


Figure 6.2 Bragg diffraction from adjacent crystal planes

For the present work, a PANalytical X'Pert Pro MRD (Materials Research Diffractometer) with a $\text{Cu K}\alpha$ X-ray source using the 2θ procedure was used to obtain the X-Ray Diffraction spectra of the Mo and Mo-N films to determine the chemical composition.

Energy Dispersive X-ray Spectroscopy (EDS) Analysis

Energy Dispersive X-ray Spectroscopy (EDS) is a technique used for determining the chemical composition of materials. It is based on the principle that each element, having a unique atomic structure generates a unique spectrum of X-rays when bombarded with an electron beam.

When an electron beam is bombarded onto a sample, X-rays are generated due to: (1) Deceleration of electrons in the coulombic field of the atom core. (2) Ejection of electrons from the inner atomic shells (3) Electrons in higher energy levels dropping to the vacancies created by ejected electrons [15].

Characteristic X-rays generated by electron transitions from higher energy levels are detected by a detector. X-rays that are generated due to electron transition from the L to the K shell are called $K\alpha$ X-rays. Similarly, $K\beta$ X-rays are generated due to M to K transitions. These shells apart from the K shell are further subdivided; for example transitions from L_1 to K generate $K\alpha_1$ X-rays, Figure 6.6 [15].

A Hitachi S-800 Scanning Electron Microscope was employed for this work to obtain the Energy Dispersive X-ray spectroscopy of the Mo and Mo-N films to determine the chemical composition of the films.

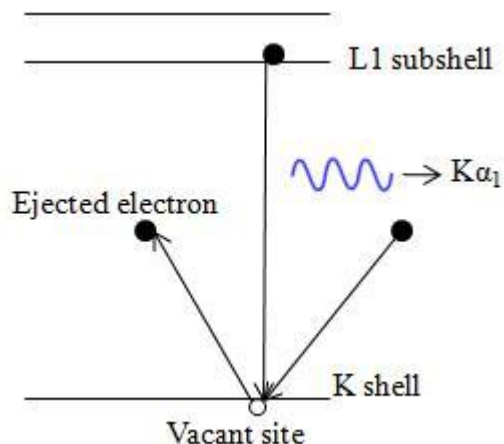


Figure 6.3 X-ray emission recorded for EDS [15]

Scanning Electron Microscopy (SEM)

Scanning Electron Microscopy is used for obtaining a magnified image of a sample. It is based on the principle that electron wavelengths being much lower than wavelengths of visible light can form high resolution images [15]. A focused electron beam incident on a sample causes ejection of (1) loosely bound secondary electrons with energies below 50eV (2) Intermediate energy auger electrons and (3) back scattered electrons with energy equivalent to the incident beam. The SEM image is formed by detecting the secondary and/or back scattered electrons. A Hitachi S-800 Scanning Electron Microscope with a 2nm resolution and 300,000X magnification was employed to obtain images of Mo and Mo-N films for this work.

RF Magnetron Sputtering

A schematic of the RF magnetron sputtering process is shown in Figure 6.2. The RF power supplied to the sputtering gun is inductively coupled to the plasma through a

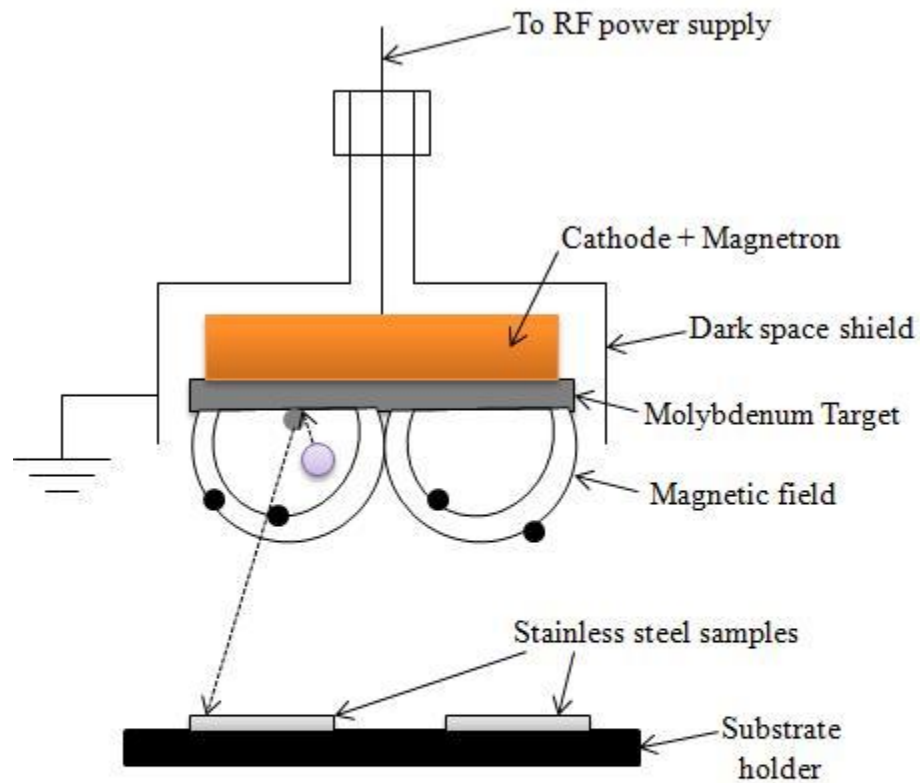
matching network which is tuned by varying the series and shunt capacitances. The RF power charges the cathode negative and positive alternatively.

An inert sputtering gas such as Ar is used if the material to be deposited is the same as the target material. In cases where oxides, nitrides or other compounds of materials are to be formed, a reactive gas is used along with the inert gas. For example to form molybdenum nitride, nitrogen is used along with inert Ar gas. This process of forming a desired compound by reaction of target material and sputtering gas is called reactive sputtering.

The physics of plasma formation is as follows: The magnetrons in the cathode create a magnetic field directly above the target surface to trap free electrons preventing them from striking the substrate and increasing the rate of reaction [74]. When electrons trapped in the magnetic field of the magnetron encounter Ar atoms, they knock off outer shell electrons from Ar atoms. The Ar⁺ ions are accelerated towards the negatively charged target and knock off molybdenum material which is deposited onto the substrate. In this process additional free electrons are created and are trapped in the magnetic field of the magnetron. Other electrons get back to the outer shell of Ar⁺ ions and the energy difference between the free electron and the bound electron is released by the Ar atom as a photon which causes the plasma to glow. This process takes place continuously. This medium of continuous energy exchange consisting of free electrons, neutral Ar atoms, Ar⁺ ions and target atoms is called plasma. [74]

A 3" TORUS® Magnetron Sputtering Cathode with a 3" Molybdenum target of 99.995% purity both from Kurt J. Lesker were used for the sputtering source. An 'RFX-

'600 RF Power Generator' was used for the RF source along with an 'ATX-600 Matching Network and Controller' from Advanced Energy Industries Inc. The flow of sputtering gases was controlled using needle valves.



- Electrons trapped by magnetic field
- Ar⁺ ions
- Molybdenum material knocked off by Ar⁺ ion

Figure 6.4 Schematic of magnetron sputtering [74]

Experimental Procedure

Sample Preparation

The SS430 stainless steel samples were ultrasonically cleaned for 45 min in acetone followed by 45 min in methanol and 45 min in de-ionized water to remove impurities on the stainless steel. Prior to deposition, the samples were again rinsed for 20 min in methanol followed by 20 min in de-ionized water to ensure an impurity free surface.

The Vacuum System

The schematic of a typical vacuum system is shown in Figure 6.5. It consists of a mechanical pump to pump the chamber to the low vacuum range of about 20mTorr and a Turbo pump to pump down to the high vacuum range of 4 – 11 μ Torr base pressure.

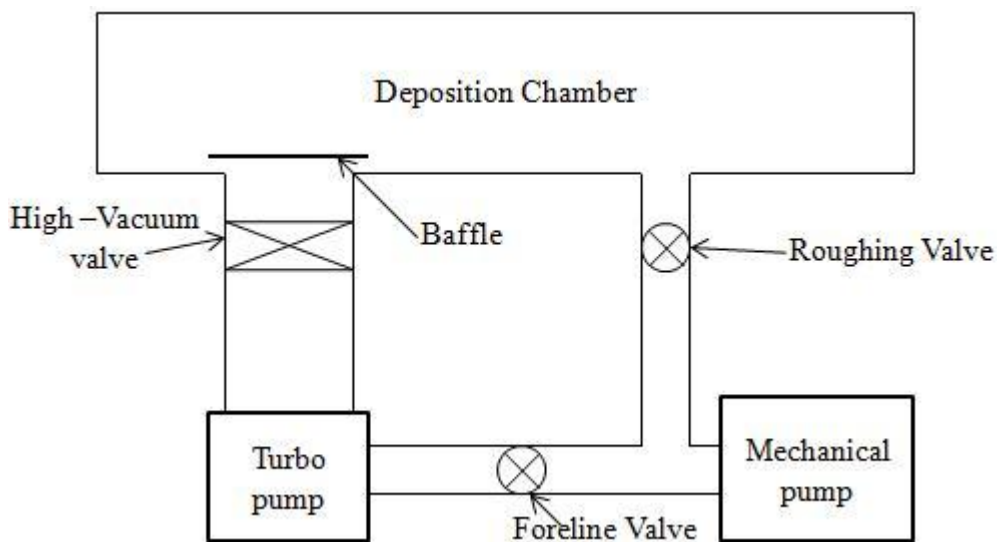


Figure 6.5 Vacuum system schematic

Spectral Response Measurement

The spectral response (SR) of a solar cell is the number of carriers collected per incident photon at each wavelength. A schematic of the experimental setup for the spectral response measurement is shown in Figure 6.5. A Cornerstone™ 260 ¼ m Monochromator is used to filter wavelengths from an Oriel Instruments Lamp (Model No. 74100). In this case wavelength from 400-900 nm which is the range of absorption for CdTe solar cells is filtered. The monochromatic light is then incident on the solar cell and the current output from the cell is measured by a Keithley 617 Programmable Electrometer controlled by LabView. A reference cell (Silicon in this case) is measured first to determine the spectral output from the monochromator, which is followed by the measurement on the CdTe solar cell. The Electrometer gives the current density output for each wavelength.

The Quantum Efficiency (Q.E) at each wavelength is known for the silicon reference cell. The current density for the silicon reference and CdTe solar cells for each wavelength is obtained from the above setup. The Q.E for the CdTe solar cell is then obtained for each wavelength as follows:

$$QE_{CdTe} = \frac{QE_{ref} * J_{CdTe}}{J_{ref}} \quad (6.4)$$

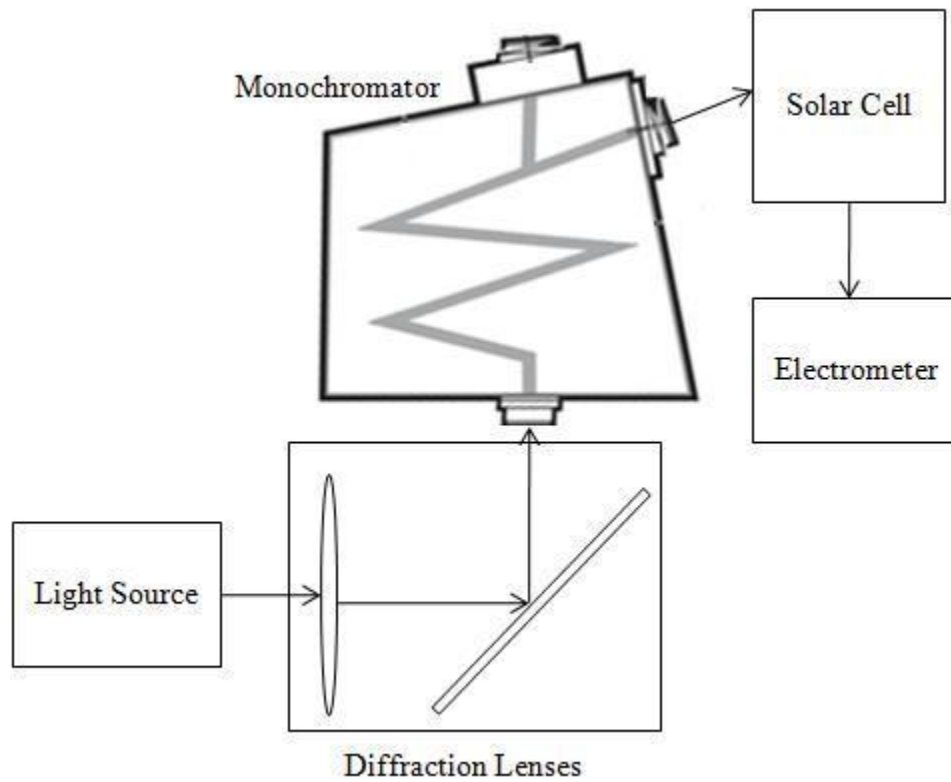


Figure 6.6 Schematic of the spectral response measurement setup [75]

J-V Measurement

AM 1.5 light from a solar simulator is shined on the solar cell of interest and a Keithley 2410 Source Meter that is controlled by LabView measures the voltage (V) and current density (J) across the solar cell and is used to obtain the J-V plot for the solar cell.

CHAPTER 7:

MOLYBDENUM NITRIDE FILMS AND SOLAR CELLS

Molybdenum and Molybdenum Nitride Thin Films by RF Magnetron Sputtering

Molybdenum (Mo) and molybdenum nitride (Mo-N) thin films were prepared in a ultra-high purity (UHP) Argon (Ar) and UHP Ar + N₂ ambient respectively by RF magnetron sputtering of a 99.995% pure Mo target. The Mo target was placed at a distance of 8cm from the substrate and the substrate was kept at RT. Though the substrate was not heated intentionally, it might have reached temperatures of about 50 – 100°C during deposition. The chamber was pumped to a base pressure of 4-11 μ Torr and initial settings of 25W and 15mTorr were used to strike plasma.

Thin Film Characterization

Rate of Deposition and Resistivity for Molybdenum Nitride Thin Films

Both Mo and Mo-N films were studied to determine the variation of deposition rate and resistivity with deposition conditions. Mo films were deposited at 250W and 9mTorr Ar. Mo-N films were deposited at two conditions: (1) 250W with a total Ar+N₂ pressure of 7mTorr and (2) 300W with a total Ar+N₂ pressure of 12mTorr. The deposition rate for Mo-N was found to be lower than the rate observed for Mo films under similar conditions of power and pressure. The deposition rate for Mo-N films

deposited at 250 and 300W for increasing N_2/Ar ratio is plotted in Figure 7.1. It can be seen that the rate increases with increasing RF power and that the rate decreases with increasing N_2 concentration in the sputtering gas. The sheet resistance and thickness of Mo and Mo-N films deposited at varying N_2/Ar ratio were measured using the 4-point probe and a DekTak thickness profilometer respectively; and the resistivity was calculated. The resistivity values of Mo-N films for different ratios of Ar and N_2 sputtering gases, deposited at 250 and 300W are shown in Table 7.1 and Table 7.2 respectively.

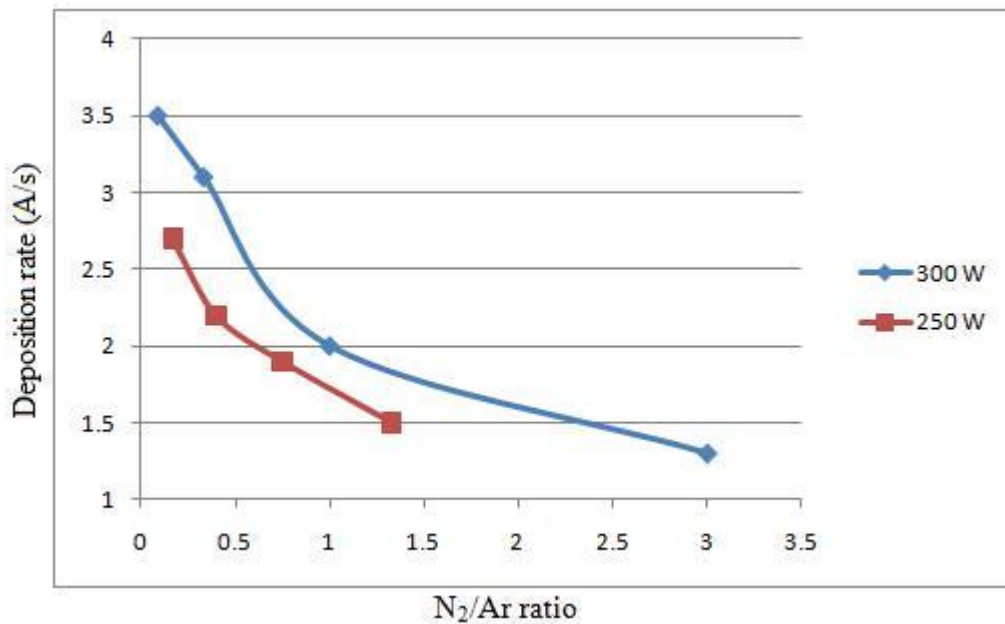


Figure 7.1 Rate of deposition for Mo-N with increasing N_2/Ar ratio

Table 7.1: Resistivity of Mo-N films deposited at 250W with increasing N₂/Ar ratio

| Ar Pressure | N ₂ Pressure | Resistivity (Ω-cm) |
|-------------|-------------------------|-----------------------|
| 6mT | 1mT | 2.45×10^{-4} |
| 5mT | 2mT | 1.08×10^{-3} |
| 4mT | 3mT | 1.00×10^{-3} |
| 3mT | 4mT | 1.50×10^{-3} |

Table 7.2: Resistivity of Mo-N films deposited at 300W with increasing N₂: Ar ratio

| Ar Pressure | N ₂ Pressure | Resistivity (Ω-cm) |
|-------------|-------------------------|----------------------|
| 11mT | 1mT | 7×10^{-4} |
| 9mT | 3mT | 2.1×10^{-3} |
| 6mT | 6mT | 9×10^{-3} |
| 3mT | 9mT | 6.3×10^{-3} |

Plain Mo films deposited at 250W power and 9mT of Ar pressure have a resistivity of 6.2×10^{-5} Ω-cm. Mo-N films deposited at 250W demonstrate as higher resistivity compared to Mo films. This might be attributed to the increased scattering of

electrons due to nitrogen present in the octahedral interstitial sites between the metal atoms as mentioned in Chapter 5, Section I; resulting in a lower mobility compared to that in the pure metal [57], [58].

A plot of the resistivity of Mo-N films deposited at 250 and 300W for different Ar and N₂ concentrations is given in Figure 7.2. The deposition rate and resistivity of Mo-N films increases with RF power for 300W compared to 250W. The resistivity of Mo-N films deposited at 300W increases with N₂ partial pressure up to a N₂/Ar ratio of 1.0, which might be attributed to the increase in nitrogen concentration in the Mo-N films as verified by Energy Dispersive X-ray Spectroscopy (EDS) measurements to be presented in this section. The resistivity of Mo-N films decreases with increase in N₂/Ar ratio greater than 1.0.

The trend in resistivity may also be attributed to the change in phase of Mo-N [76]. With very low N₂ partial pressures, XRD analysis indicates the presence of cubic Mo₃N₂. When the N₂ partial pressure is increased, the Mo₅N₆ phase is observed and for N₂/Ar ratio of 1.0, the hexagonal δ -MoN is observed. Increasing the N₂ partial pressure further causes a decrease in intensity and broadening of the MoN peak. The change of Mo-N phase with N₂ concentration is shown in the XRD spectra on pages 47 and 48. It can be deduced that the resistivity of Mo-N films is highest for films which are composed predominantly of δ -MoN.

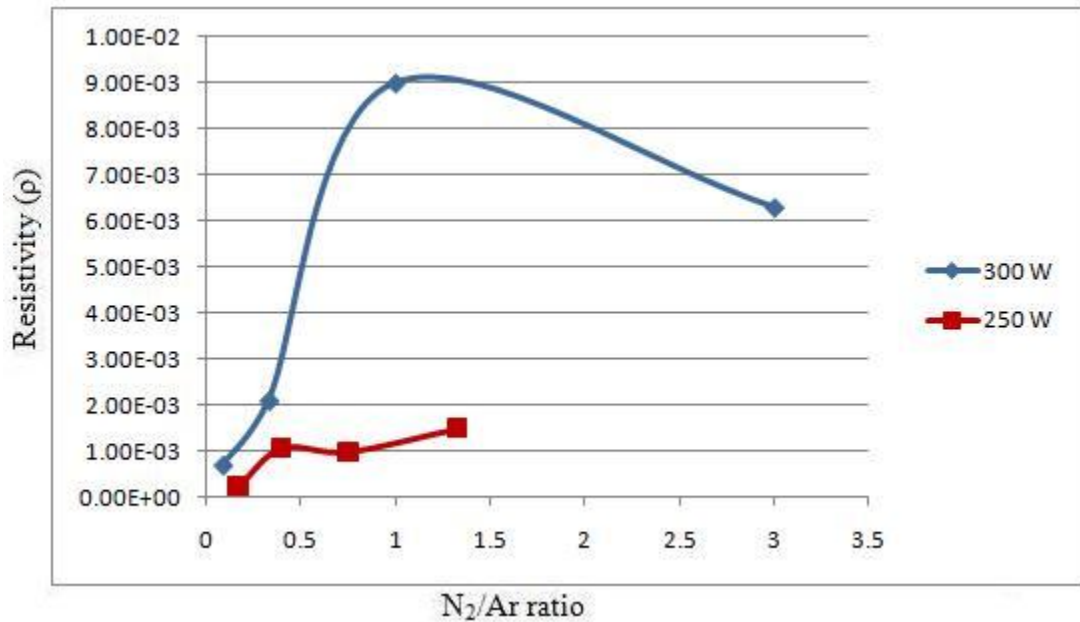


Figure 7.2 Resistivity of Mo-N with increasing N₂/Ar ratio

X-Ray Diffraction Spectroscopy (XRD) Analysis

X-Ray diffraction (XRD) spectroscopy was performed on the Mo-N films to identify the microstructure, phase and composition of the films.

The XRD graphs of a Mo film deposited at 250W and Mo-N films deposited at 300W along with the percentage of N₂ in the sputtering gas are shown in Figure 7.3. The Mo-N films change in phase with different ratio of Argon and Nitrogen partial pressures, with the Mo₂N phase of molybdenum nitride being present for all Nitrogen concentrations. The Mo₂N and MoN phases are identified as β-Mo₂N and δ-MoN from the crystal structure and lattice constants reported in the literature [64], [68], [72]. For very low nitrogen concentrations of 9.09% in the sputtering gas, cubic Mo₃N₂ is formed and transforms to hexagonal Mo₅N₆ for 25% N₂. Increasing the N₂ concentration to 50%,

results in a strong hexagonal δ -MoN peak. For higher N_2 concentrations, Mo-N films show reduced peak intensity with a wider peak width. Most of the Mo-N peaks obtained from the films deposited by us did not align perfectly with the peaks from PDF files. The error corresponding to the dominant peaks is given as ‘ 2θ error’ in Table 7.3.

$$2\theta \text{ error} = \frac{\text{measured } 2\theta - 2\theta \text{ from PDF}}{2\theta \text{ from PDF}} \quad (7.1)$$

The lattice parameters and crystal orientation of the different phases of molybdenum nitride obtained from the PDF files that correspond to these peaks are shown in Table 6.4 for the dominant peaks observed around 2θ of 36 and 43°.

XRD graphs of Mo-N films deposited at 250W are shown in Figure 7.4 along with the concentration of N_2 in the sputtering gas in each case. At 57.14 % N_2 in the sputtering gas, the films appear to become amorphous or tending to be nano-crystalline. The intensity of the Mo_2N peaks decreases with increasing N_2 concentration. The transformation in phase of Mo-N with increasing N_2 concentration is similar to that observed for Mo-N films deposited at 300W. However, the intensity of the MoN peak reduces drastically with increase in N_2 concentration from 42.9 to 57.14%.

Bull et al. have determined that the nitrogen and molybdenum sites are fully occupied for the highly ordered δ -MoN phase with lattice parameters of $a = 5.73659 \text{ \AA}$ and $c = 5.61884 \text{ \AA}$ [72]. The XRD peaks corresponding to the δ -MoN phase observed in Figures 7.3 and 7.4 have lattice constants of $a = 5.74 \text{ \AA}$ and $c = 5.622 \text{ \AA}$, which are very close to those reported by Bull et al., which suggest the formation of a highly ordered δ -MoN phase.

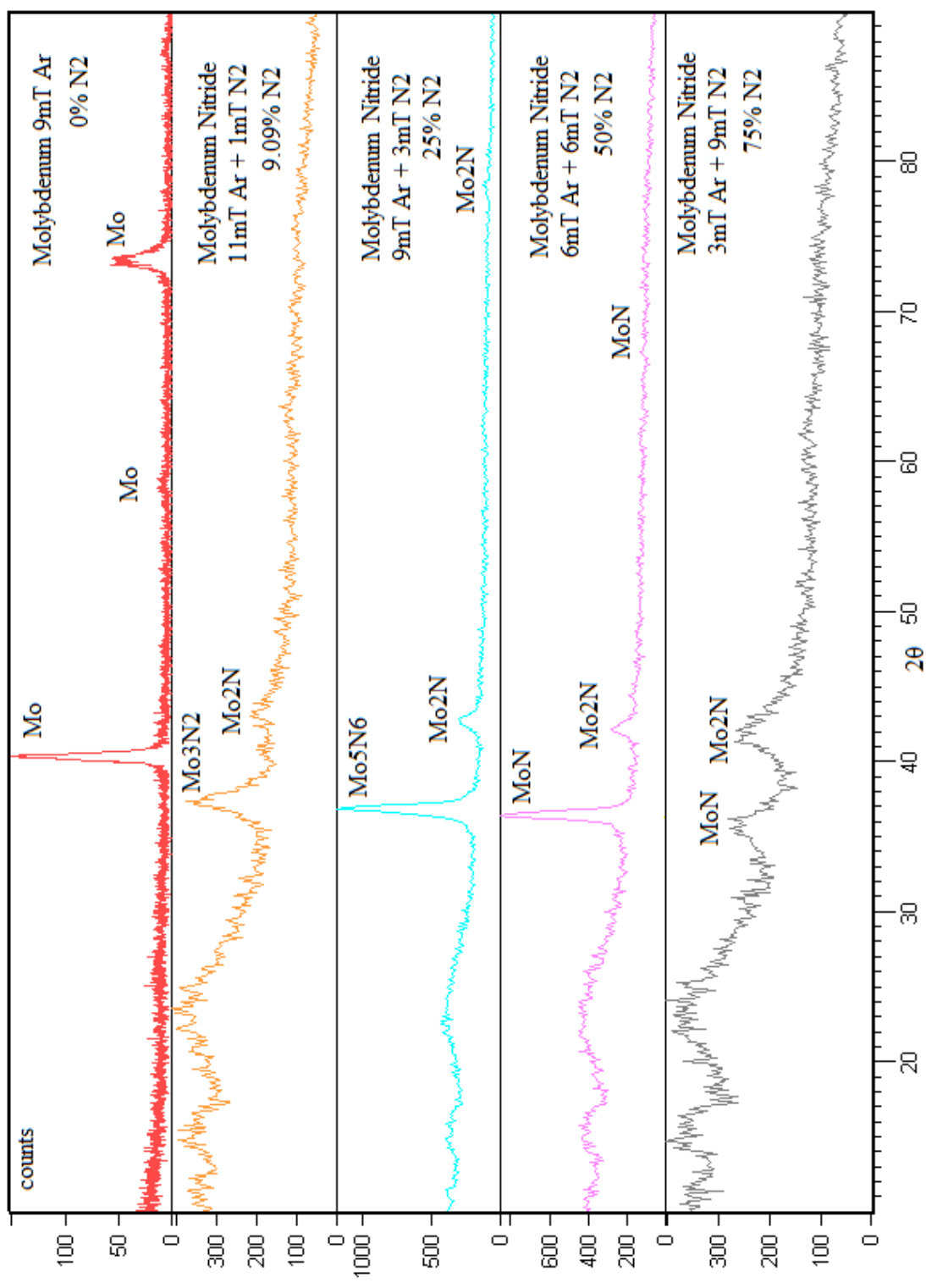


Figure 7.3 XRD spectra of Mo and Mo-N films deposited at 300W

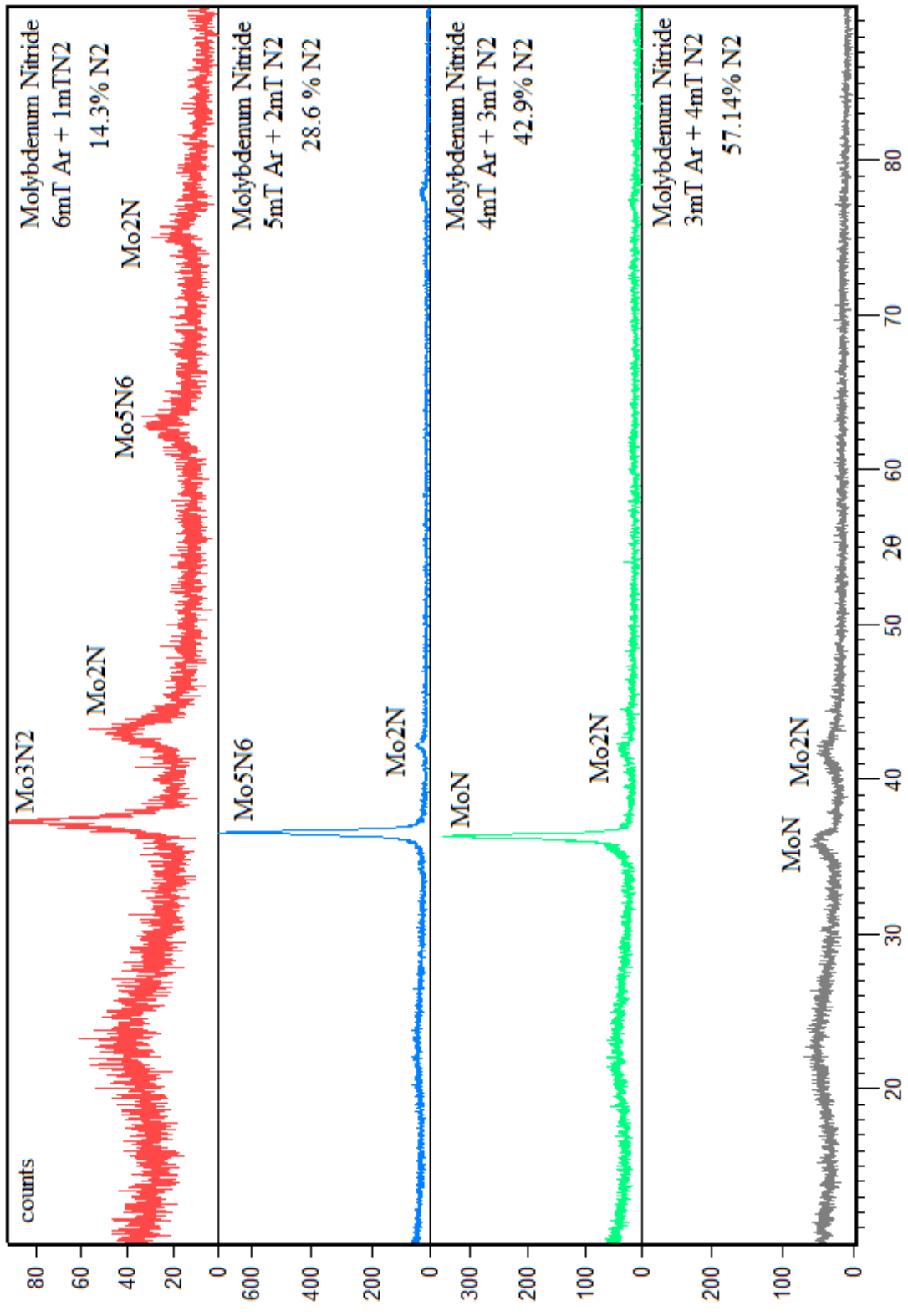


Figure 7.4 XRD spectra of Mo-N films deposited at 250W

Table 7.3 Crystal parameters of various phases of Molybdenum Nitride

| Phase | Crystal structure | Lattice parameters (Å) | Orientation | 2θ error (Degrees) |
|--------------------------------|-------------------|---------------------------|-------------|-----------------------|
| Mo ₃ N ₂ | Cubic | a = 4.165 | (111) | -0.0030 |
| β Mo ₂ N | Tetragonal | a = 4.2, c = 8.0 | (200) | -0.0046, -0.0056 |
| Mo ₅ N ₆ | Hexagonal | a = 4.893, c = 11.06 | (110) | -0.0057, -0.0001 |
| δ MoN | Hexagonal | a = 5.74, c = 5.622 | (200) | -0.0030 |

Energy Dispersive X-ray Spectroscopy (EDS) Analysis

The composition of Mo and Mo-N films deposited for varying N₂/Ar ratios were determined using EDS at electron beam energy of 5kV. The Kα energy of Nitrogen is 0.392 keV and 0.523 keV for Oxygen. Mo has a Kα energy of 17.443 keV and an Lα₁ energy of 2.293 keV. The results of the analysis are shown in Table 7.4 and Figure 7.5.

Table 7.4 Composition of films determined by EDS

| Film | Ar partial pressure (mTorr) | N ₂ partial pressure (mTorr) | Mo at. % | N at. % | O at. % |
|------|-----------------------------|---|----------|---------|---------|
| Mo | 9 | 0 | 91.21 | 0.00 | 8.79 |
| Mo-N | 9 | 3 | 86.06 | 9.53 | 4.41 |
| Mo-N | 6 | 6 | 60.37 | 34.34 | 5.29 |
| Mo-N | 3 | 9 | 60.25 | 35.86 | 3.9 |

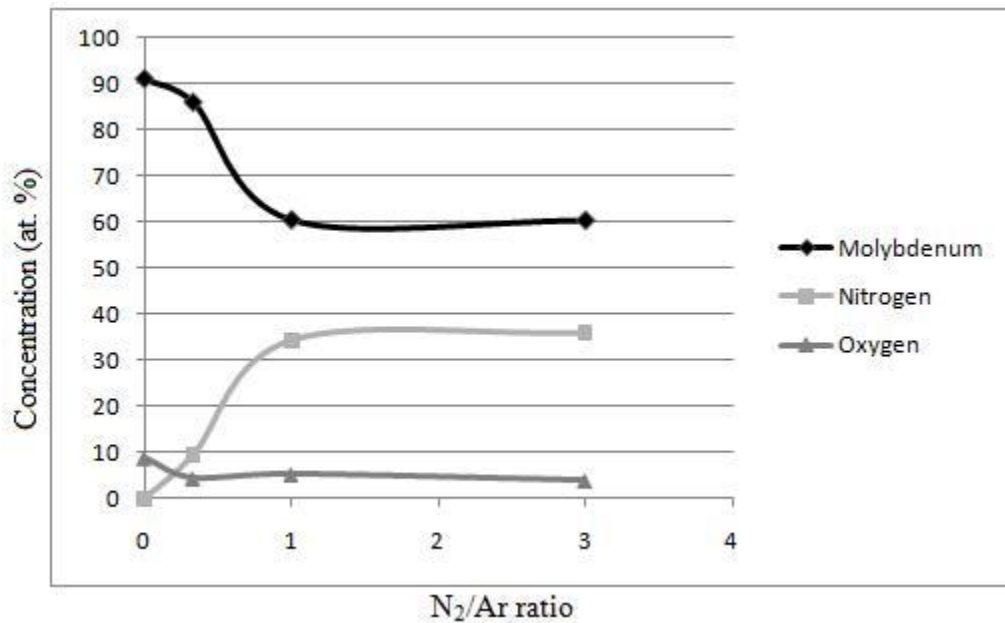


Figure 7.5 Variation of atomic percentage of Mo, N and O by EDS

It can be inferred from Table 7.4 that the atomic percentage (at. %) of nitrogen in the Mo-N films increases with increasing N₂ partial pressure in the sputtering gas. However, beyond 50% N₂ in the Ar+N₂ gas, the nitrogen at. % appears to saturate and increases by less than 5% for 75% N₂. The Oxygen atomic percentage in the films doesn't seem to follow any trend. It appears that Mo films tend to have a higher oxygen concentration when compared to Mo-N films.

Scanning Electron Microscopy (SEM) Analysis

SEM images of Mo film deposited at 250W and Mo-N films deposited at 300W are shown in Figure 7.6 (a) – (d). No grain structure is observed in the Mo film. The Mo-N film deposited with 25% N₂ in the sputtering gas has a grain size of about 50nm as seen in Figure 7.6 (b). At N₂ concentrations of 50%, no grain structure is observed at 130K magnification. The Mo-N film deposited at 50% N₂ appears to have a surface morphology similar to the STM images of δ -MoN by R. Sanjinés et al [77]. Films with 75% N₂ concentration have spherical grains with size of about 50nm randomly scattered over the film.

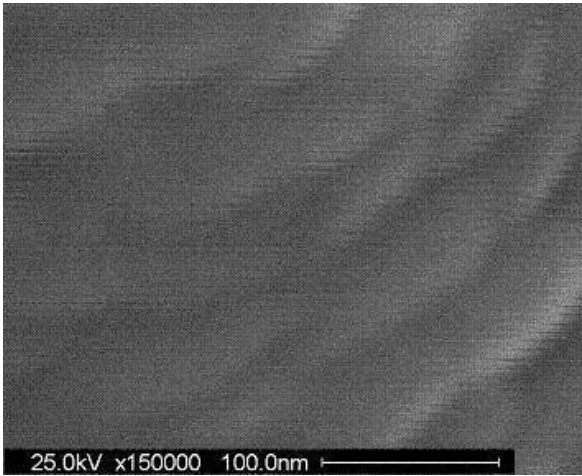
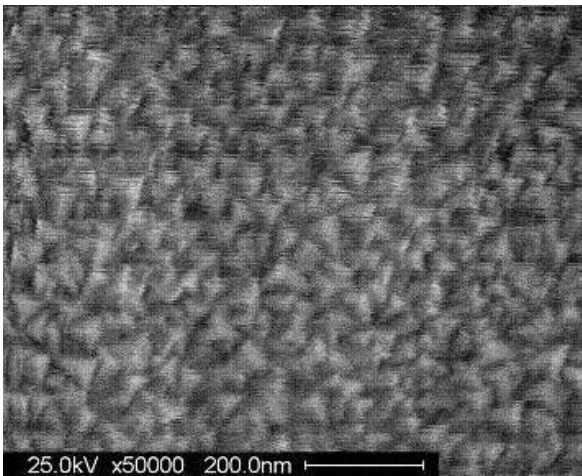
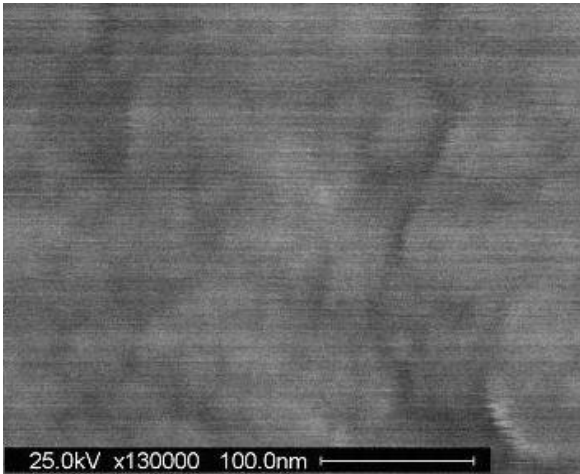


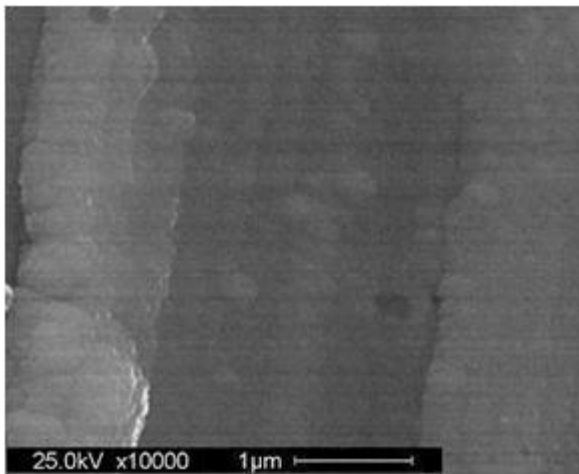
Figure 7.6 SEM images of Mo and Mo-N films (a) Mo film at 150K magnification



(b) Mo-N film deposited at 9mTorr Ar + 3mTorr N₂ at 50K magnification



(c) Mo-N film deposited at 6mTorr Ar + 6mTorr N₂ at 130K magnification



(d) Mo-N film deposited at 3mTorr Ar + 9mTorr N₂ at 10K magnification

Solar Cells with Molybdenum Nitride Back Contacts

In this section, solar cells contacted with molybdenum only as the back contact metal and solar cells involving Mo-N in the back contact structure will be compared and the performance of these cells will be discussed.

J-V measurements with and without Molybdenum Nitride Back Contacts

Solar cells employing Mo-N in the back contact structure were made on stainless steel (SS) substrates of SS430 alloy, in the following configurations:

SS/Mo/Mo-N/CdTe/CdS/TC,

SS/Mo-N/Mo/Mo-N/CdTe/CdS/TC,

SS/Mo/Mo-N/Mo/CdTe/CdS/TC

TC in the above configurations denotes Transparent Contact which was ITO based demonstrating a sheet resistance of about 8-10 Ω/\square . All the Mo layers used in CdTe solar cells were deposited at 250W and 9mTorr of Ar pressure and all Mo-N layers were deposited at 300W with the total pressure of (Ar+N₂) kept constant at 12mTorr.

A comparison of J-V curves for the standard '*SS/Mo/CdTe/CdS/TC*' structure and the '*SS/Mo/Mo-N/CdTe/CdS/TC*' structure with Mo-N deposited at 6mTorr Ar + 6mTorr N₂ is shown in Figure 7.7 with a comparison of cell parameters given in Table 7.5. The use of the Mo-N layer appears to cause an increase in the FF and the V_{oc} of the cells and a small decrease in the J_{sc}, Table 7.5. The improved performance of solar cells with Mo/Mo-N as the back contact compared to those with only Mo as the back contact is expected to be because of the Mo grain boundaries being stuffed by nitrogen and reducing diffusion along grain boundaries accompanied by a reduction in grain size thereby acting as better barriers [78], [79]. Mo-N has been previously proved to be a

good diffusion barrier by many authors against diffusion of Al, Cu and Au in Si [80], [81], [82], [83], [79].

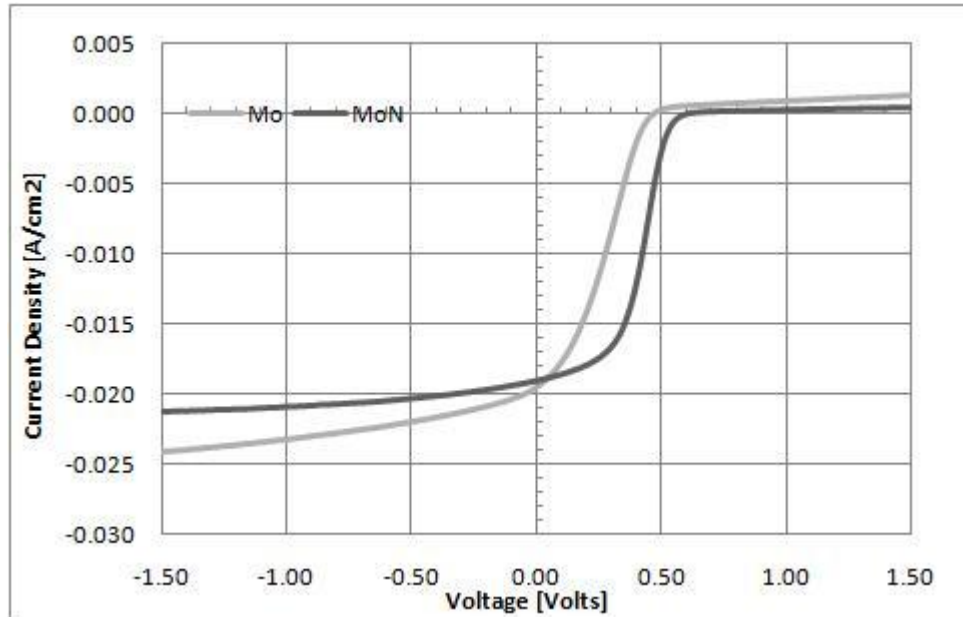


Figure 7.7 J-V curves for solar cells with Mo versus Mo/MoN for the back contact

Table 7.5 Comparison of performance of solar cells with Mo and MoN back contacts

| Structure | N ₂ partial pressure | Ar partial pressure | V _{oc} (mV) | FF (%) | J _{sc} (mA/m ²) |
|-----------------------|---------------------------------------|---------------------------|-------------------------|-----------|--------------------------------------|
| SS/Mo/MoN/CdTe/CdS/TC | 0mT | 9mT | 600 | 46 | 19.04 |
| SS/Mo/CdTe/CdS/TC | 6mT | 6mT | 400 | 42 | 19.46 |

Solar cells with the structure ‘SS/Mo/Mo-N/CdTe/CdS/TC’ have been fabricated with Mo-N layers deposited at different ratios of N₂/Ar partial pressures. A comparison of the J-V curves for these solar cells is shown in Figure 7.7. The efficiencies obtained for cells with 9mTorr Ar + 3mTorr N₂, 6mTorr Ar + 6mTorr N₂, 3mTorr Ar + 9mTorr N₂ are 4.26%, 4.91% and 3.45% respectively. The V_{oc}, FF and efficiency for different N₂/Ar ratios are shown in Table 7.6. All Mo-N based cells show a better performance when compared to Mo based cells. Of the Mo-N based cells, the cells with 6mTorr Ar + 6mTorr N₂ Mo-N films show a better performance compared to cells with Mo-N films deposited at other Ar and N₂ compositions. This can be attributed to the presence of δ-MoN. Highly dense, stable and ordered films act as good barriers because of reduced diffusion through defects, vacancies or reaction with adjoining layers [84]. Hence, the presence of the densely packed, highly ordered and thermodynamically stable δ-MoN in the Mo-N film deposited at 50% N₂ could be the reason for it to act as a better barrier to diffusion of impurities from the stainless steel substrates due to subsequent high temperature processing [71], [72]. It has also been shown that the total energy of δ-MoN is lower than cubic Mo-N, causing it to be more stable [85]. The Mo-N films deposited at 75%N₂ have a lower intensity δ-MoN peak compared to those deposited at 25%, which might be the reason for poorer performance. It has been shown that nano-crystalline or amorphous layers act as better diffusion barriers with no grain boundaries for impurities to diffuse along [86], [87], [88], [89]. The Mo-N layer deposited at 6mTorr Ar + 6mTorr N₂ might be performing better because of having a nano-crystalline structure which might not have been observable in the SEM images; but this has to be verified by high resolution transmission electron microscopy (HRTEM).

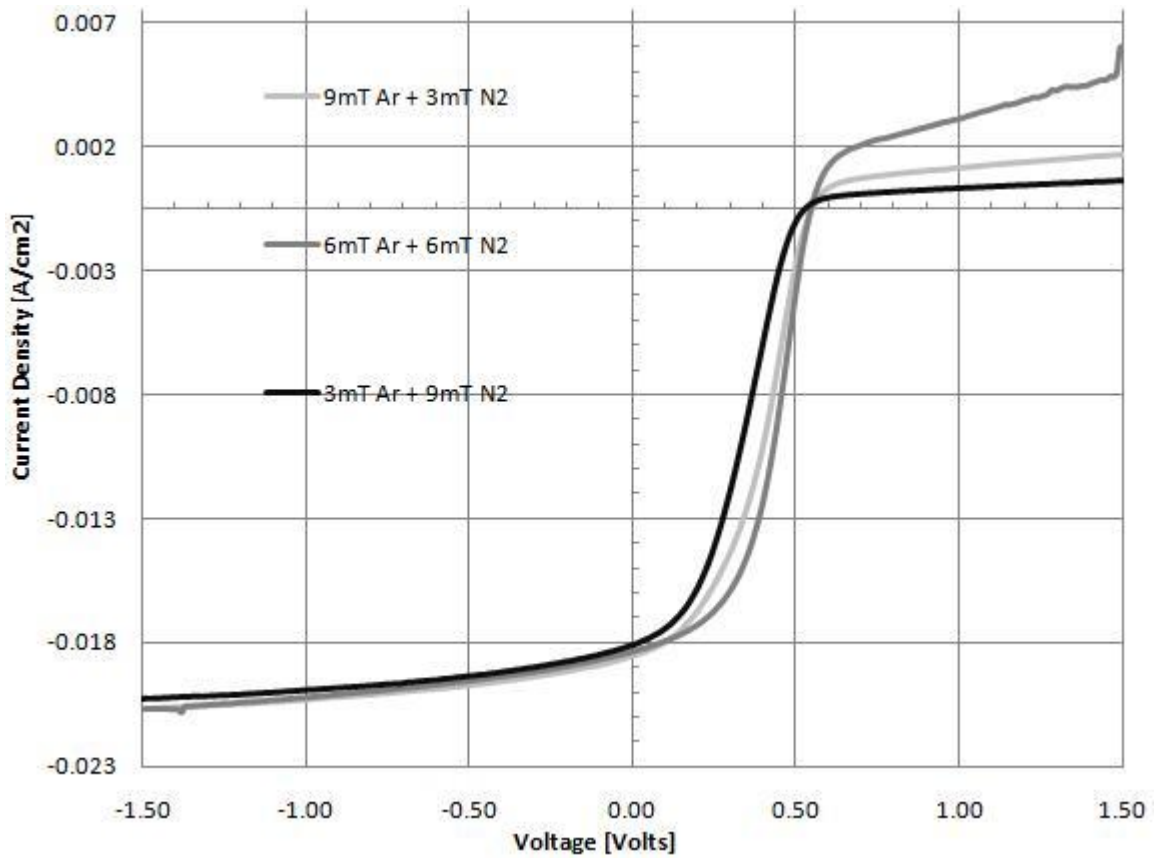


Figure 7.8 J-V curves for solar cells with varying N₂ and Ar pressures

Table 7.6 Solar cell characteristics for varying N₂ concentration for cells with ‘SS/Mo/Mo-N/CdTe/CdS/TC’ configuration

| N ₂ partial pressure | Ar partial pressure | V _{oc} (mV) | FF (%) | J _{sc} (mA/m ²) |
|---------------------------------|---------------------|----------------------|--------|--------------------------------------|
| 3mT | 9mT | 550 | 43 | 18.01 |
| 6mT | 6mT | 540 | 51 | 17.83 |
| 9mT | 3mT | 530 | 37 | 17.61 |

Solar cells have also been made for possible improvements in performance in the following configurations:

SS/Mo-N/Mo/Mo-N/CdTe/CdS/TC,

SS/Mo/Mo-N/Mo/CdTe/CdS/TC

All solar cells manufactured with the above configuration employed Mo-N layers with 6mT Ar + 6mT N₂ in the sputtering gas. J-V plots for cells with these configurations are shown in Figure 7.8 with cell parameters given in Table 7.7. The solar cells with the Mo-N/Mo/Mo-N back contact structure show better performance compared to cells with Mo/Mo-N/Mo.

Comparing the various cells made with different configurations of Mo-N shows that the Mo/Mo-N back contact structure performs better.

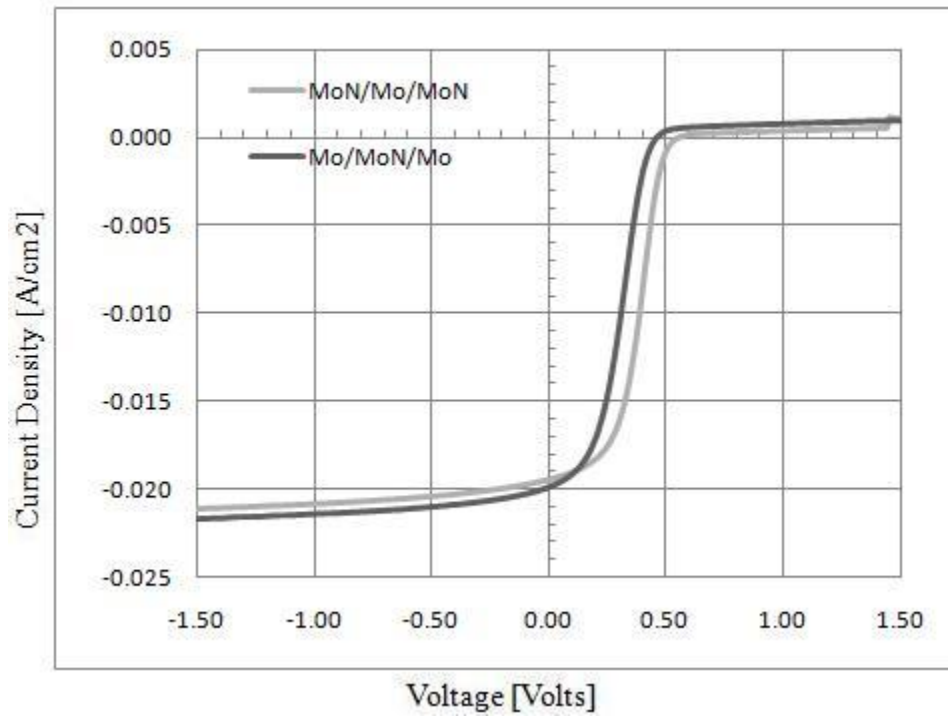


Figure 7.9 J-V measurements of solar cells with Mo-N/Mo/Mo-N and Mo/Mo-N/Mo stack used as back contacts.

Table 7.7 Solar cell characteristics for cells with the stack as back contact

| Structure | V_{oc} (mV) | FF (%) | J_{sc} (mA/m ²) |
|---------------------------|------------------|-----------|----------------------------------|
| SS/Mo/MoN/Mo/CdTe/CdS/TC | 440 | 43 | 19.83 |
| SS/MoN/Mo/MoN/CdTe/CdS/TC | 500 | 47 | 19.42 |

Spectral Response Measurements of CdTe Solar Cells with Molybdenum Nitride in the Back Contact Structure.

A plot of the spectral response (SR) for cells employing Mo and Mo/Mo-N for the back contact structure, with the Mo-N film deposited at 50% N₂ is shown in Figure 7.9. There is no observable difference in the Quantum Efficiency (Q.E) plot of the two cells.

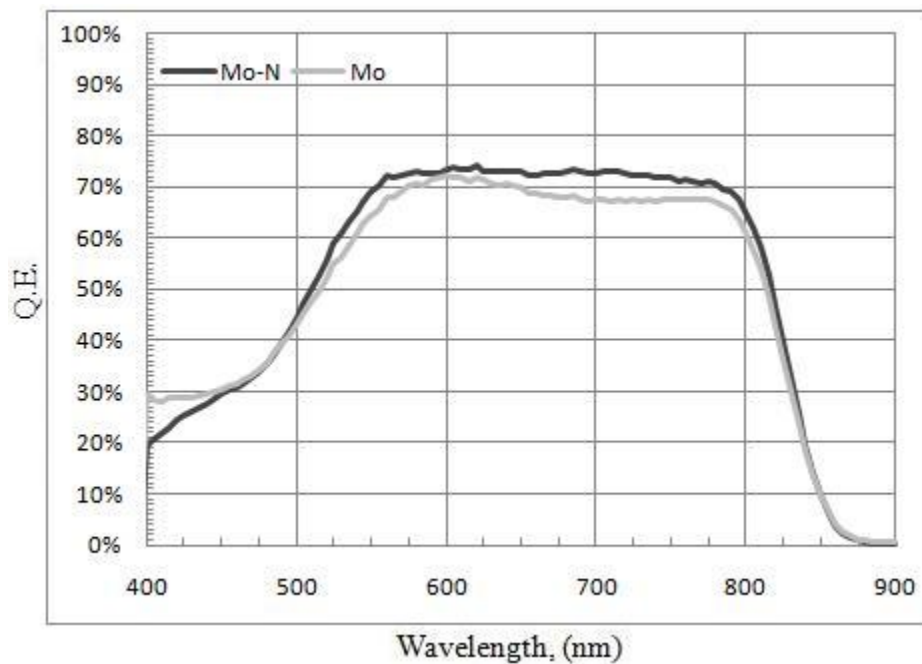


Figure 7.10 SR curves of solar cells with Mo and Mo/Mo-N used as back contacts.

Solar Cell Efficiency

The efficiencies for solar cells with different back contact structures have been calculated, and the cells involving Mo-N in the back contact structure exhibited higher efficiencies compared to cells employing only Mo for the back contact. The Mo/Mo-N back contacted cells recorded an efficiency of 5.26%, which is the highest obtained in the

present work, when compared to 3.27 % for cells employing only Mo in the back contact keeping all other factors the same. Mo-N back contacted cells exhibited an efficiency of 4.75 % on an average.

Work Function of Mo-N

The work function of MoN is reported in the literature to be between 4.7 - 5.33eV and that for Mo is 4.64eV [90], [91], [92]. The work function of CdTe is around 5.95eV. The Mo-N layer does not seem to show any noticeable improvement in the reduction of the back contact barrier height from the I-V curves [26].

Nitrogen Incorporation into CdTe

Nitrogen incorporation into CdTe would lead to p+ doping of CdTe near the metal contact. The high decomposition temperature of Mo-N (Mo_2N decomposes at 790°C) [93], [94]. The highest temperatures employed for depositing the layers in CdTe solar cells after the back contact in the present case are around 460°C. Hence, the chances of Mo-N decomposing and causing nitrogen to be incorporated into CdTe are very unlikely.

CHAPTER 8:

CONCLUSIONS AND FUTURE WORK

Conclusions

CdTe solar cells with Molybdenum Nitride in the back contact structure consistently demonstrated better performance when compared to cells with only Molybdenum as the back contacts. It is possible that the improved performance of Mo-N based cells is due to the diffusion barrier property of the Mo-N layer due to stuffing of Mo grain boundaries by nitrogen accompanied by a decrease in grain size, reducing the chances of diffusion along grain boundaries [78], [79]. The performance of CdTe solar cells is found to be the best for Mo-N films deposited at 6mTorr Ar + 6mTorr N₂ (50% N₂). This can be attributed to the presence of the densely packed, highly ordered, thermodynamically stable δ -MoN, since highly ordered, dense and stable films act as better barriers because of low defects, vacancies and low reactivity [71], [72], [84]. The higher stability of δ -MoN has been attributed to its low total energy [85]. Hence it is expected that the Mo-N layer acts as a diffusion barrier to Fe and Cr impurities from the stainless steel substrate.

The improvement of cell performance due to the higher work function of MoN (4.7-5.33 eV) compared to Mo (4.64 eV) is considered unlikely because of no noticeable

improvement in the I-V curve. The chances of nitrogen incorporation into CdTe resulting in p-doped CdTe are less because of highest processing temperatures of about 650°C and due to high decomposition temperatures of Mo-N [94].

Future Work

The use of Mo-N in the back contact structure has improved CdTe solar cell efficiency. This has been attributed to Mo-N acting as a diffusion barrier. The following work is suggested to support the above claim.

- SIMS measurements of Mo and Mo-N back contacted solar cells would give an indication of the extent of diffusion of Fe and Cr in these cells.
- High resolution Transmission Electron Microscopy (HRTEM) imaging might help observe microstructures that might not have been observed in the SEM images.

The following are suggested to increase the understanding of Mo-N back contacts in CdTe solar cells.

- Mo-N films deposited at 3mT Ar + 4mT N₂ at 250W appear to tend to be amorphous and it might be interesting to employ this layer as a barrier.
- Increasing the thickness of the Mo-N layer in cells with Mo-N/Mo back contact structure might be helpful.

- Annealing of Mo-N layers or deposition of Mo-N layers in the SS/Mo/Mo-N/CdTe/CdS/TC structure might result in better cell performance and should be studied.

REFERENCES

- [1] U.S Energy Information Administration, "Figure 2. World marketed energy use by fuel type (quadrillion Btu)", DOE/EIA-0484(2010) (May 25 2010).
- [2] BP Statistical Review of World Energy 2010 workbook.
- [3] Nathan S. Lewis, George Crabtree, "Basic Research Needs for Solar Energy Utilization", Report of the Basic Energy Sciences Workshop on Solar Energy Utilization, , April 18 -21, 2005.
- [4] Arnulf Jäger-Waldau, PV Status Report 2009.
- [5] Robert F. Service, Is It Time to Shoot for the Sun? Science 22. 309 no.5734 (July 2005) 584-551.
- [6] Martin A. Green, Solar Cells Operating Principles, Technology, and System Applications.
- [7] Martin A. Green, Third Generation Photovoltaics: Advanced Solar Energy Conversion.
- [8] Gavin Conibeer, Third generation photovoltaics, Materials Today. 10 (November 2007) 42 - 50.
- [9] Lawrence Kazmerski, Best Research-Cell Efficiencies, NREL.
- [10] Tom Key, "Solar Photovoltaics *Expanding Electric Generation Options*", Electric Power Research Institute, (December 2007).
- [11] S. M. Sze, Physics of Semiconductor Devices.
- [12] R. F. Pierret, Semiconductor Device Fundamentals.
- [13] E. H. Rhoderick, R. H. Williams, Metal - Semiconductor Contacts.
- [14] John Bardeen, Surface states and rectification at a metal-semiconductor contact. Physical Review. 71 (May 15, 1947).

- [15] Dieter K. Schroder, Semiconductor Material and Device Characterization, Third Edition ed.
- [16] W. E. Spicer et al, The Unified Model for Schottky Barrier Formation and MOS Interface States in 3-5 Compounds, Applied Surface Science. 9 (Sept 1981) 83-91.
- [17] Raymond T. Tung, Schottky Barrier Height Tutorial (NSF Funded).
- [18] Alan L. Fahrenbruch, Ohmic Contacts and doping of CdTe, Solar Cells. (1987).
- [19] J. P. Ponpon, A review of ohmic and rectifying contacts on cadmium telluride. Solid State Electronics. 28 (1985) 689-706.
- [20] P.M. Dieter Bonnet, Cadmium-telluride—Material for thin film solar cells, Journal of Materials Research. 13 (October 1998).
- [21] NASA Glenn Research Center at Lewis Field, Chemical Fabrication used to produce thin-film materials for high power-to-weight-ratio space photovoltaic arrays, in: Anonymous 1999 Research & Technology, NASA/TM-2000-209639.
- [22] P. D. Paulson et al, Study of in situ CdCl₂ treatment on CSS deposited CdTe films and CdS/CdTe solar cells, Thin Solid Films. 370 (2000) 299-306.
- [23] Kenneth Zanio, Semiconductors and Semimetals, Volume 13, "Cadmium Telluride".
- [24] Xavier Mathew et al, CdTe/CdS solar cells on flexible substrates, Solar Energy. 77 (2004) 831.
- [25] Ilvydas Matulionis et al, Cadmium Telluride Solar Cells on Molybdenum Substrates, Materials research society. (2001 Spring).
- [26] S. H. Demtsu and J. R. Sites, Effect of back-contact barrier on thin-film CdTe solar cells, Thin Solid Films. 510 (2006) 320-324.
- [27] N. Romeo et al, A highly efficient and stable CdTe/CdS thin film solar cell, Solar Energy Materials and Solar Cells. 58 (June 1999) 209-218.
- [28] J. Britt and C. Ferekides, Thin-film CdS/CdTe solar cells with 15.8% efficiency, Applied Physics Letters. 62 (31 May 1993) 2851-2852.
- [29] S. K. Das and G. C. Morris, Influence of growth and microstructure of electrodeposited cadmium telluride films on the properties of n-CdS/p-CdTe thin-film solar cells, J. Appl. Phys. 72 (15 November 1992).

- [30] N. Suyama et al, CdS/CdTe solar cells by the screen-printing-sintering technique, (1990) 498-503.
- [31] H. C. Chou et al, Effects of Cu on CdTe/CdS heterojunction Solar Cells with Au/Cu Contacts, *J. Electrochem. Soc.*, Vol. 142, No. 1, January 1995.
- [32] D. L. Bätzner et al, A study of the back contacts on CdTe/CdS solar cells, *Thin Solid Films*. 361-362 (21 February 2000) 463-467.
- [33] B. Ghosh et al, Formation of a stable ohmic contact to CdTe thin films through the diffusion of P from Ni-P, *Semiconductor Science and Technology*. 10 (1995) 71-76.
- [34] V. Viswanathan et al, Ni₂P- A promising candidate for back contacts to CdS/CdTe Solar Cells, *Conference Record, IEEE Photovoltaics Specialists Conference*. 28 (2000) 587-590.
- [35] R. B. Hall, H. H. Woodbury, The Diffusion and Solubility of Phosphorus in CdTe and CdSe, *Journal of Applied Physics*. 39 (November 1968) 5361-5365.
- [36] A. Aoudia et al, Crystal growth and characterization of CdTe doped with transition metal elements, *Optical Materials*. 4 (1995) 241-245.
- [37] H. L. Hwang et al, Fundamental studies of p-type doping of CdTe, *Journal of Crystal Growth*. 161 (1 April 1996) 73-81.
- [38] Billy L. Crowder and William N. Hammer, Shallow Acceptor States in ZnTe and CdTe, *Physical Review*. 150 (14 October 1966).
- [39] F. A. Selim, F. A. Kroger, The Defect Structure of Phosphorus-Doped CdTe, *Journal of the Electrochemical Society*. 124 (1977) 401-410.
- [40] Thomas C. Anthony et al., Electrical properties of CdTe films and junctions, *Journal of Applied Physics*. 57 (January 1985) 400-410.
- [41] Y. Marfaing, Impurity doping and compensation mechanisms in CdTe, *Thin Solid Films*. 387 (2001) 123-128.
- [42] V. S. John et al, Synthesis and characterization of copper doped zinc telluride thin films, *Solid-State Electronics*. 49 (January 2005) 3-7.
- [43] T. L. Chu et al, Deposition and characterization of p-type cadmium telluride films, *Journal of Applied Physics*. 58 (August 1985) 1349-1355.
- [44] H Zhao et al, The effect of impurities on the doping and VOC of CdTe/CdS thin film solar cells, *Thin Solid Films*. 517 (2 February 2009) 2365-2369.

- [45] T. L. Chu et al, 13.4% efficient thin-film CdS/CdTe solar cells, *J. Appl. Phys.* 70 (Dec 1991) 7608-7612.
- [46] Bulent M. Basol, Electrodeposited CdTe and HgCdTe solar cells, *Solar Cells.* 23 (Jan-Feb 1988) 69-88.
- [47] M. Florez et al, Low resistance contact to CdTe thin films.
- [48] J. H. Yun et al, Back Contact formation using Cu₂Te as a Cu-doping source and as an electrode in CdTe solar cells, *Solar Energy Materials and Solar Cells.* 75 (2003) 203-210.
- [49] D. L. Bätzner et al, Development of efficient and stable back contacts on CdTe/CdS solar cells, *Thin Solid Films.* 387 (2001).
- [50] D. Rioux et al, ZnTe: a potential interlayer to form low resistance back contacts, *J. Appl. Phys.* 73 (15 June 1993) 8381-8385.
- [51] F Kitagawa et al, Molecular Beam Epitaxial Growth of ZnTe and ZnSe, *J. Electrochem. Soc.* 127 (April 1980) 937-943.
- [52] T. M. Duc et al, Linearity (commutativity and transitivity) of valence-band discontinuity in heterojunctions with Te-based II-VI semiconductors: CdTe, HgTe, and ZnTe, *Phys. Rev. Lett.* 58 (16 March 1987) 1127-1130.
- [53] J. Tang et al, The Properties and Optimization of ZnTe:Cu Back Contacts on CdTe/CdS Solar Cells, 925-928.
- [54] T. A. Gessert, Effects of Cu from ZnTe:Cu contacts in CdS/CdTe cells, 654 - 657.
- [55] V. P. Singh et al, Thin film CdTe-CdS heterojunction solar cells on lightweight metal substrates, *Solar Energy Materials and Solar Cells.* 59 (1999) 145-161.
- [56] J. P. Enríquez, CdTe/CdS Solar cells on flexible molybdenum substrates, *Solar Energy Materials and Solar Cells.* 82 (2004).
- [57] S. Ted Oyama, S. Kikkawa et al., Transition metal-based double nitrides, The chemistry of transition metal carbides and nitrides, in: Anonymous.
- [58] Louis E. Toth, *Transition Metal Carbides and Nitrides.*
- [59] P.E. H. Jehn, The Molybdenum-Nitrogen phase diagram, *Journal of the Less-Common Metals.* 58 (1978) 85 - 98.

- [60] T. B. Massalski, H. Okamoto, Binary Alloy Phase Diagrams, in: Anonymous , pp. 2631, 2632.
- [61] J. H. Evans and K. H. Jack, Acta Crystallogr. 10 (1957) 833.
- [62] D. A. Evans and K. H. Jack, The $\gamma \rightarrow \beta$ phase transformation in the Mo-N system.
- [63] P. Ettmayer, Monatsh. Chem. 101 127.
- [64] K. Inumaru et al, Synthesis and Characterization of Superconducting β -Mo₂N crystalline phase on a Si substrate: An application of Pulsed Laser Deposition to Nitride Chemistry, Chemistry of Materials. 17 (2005) 5935-5940.
- [65] N. V. Troitskaya and Z. G. Pinsker, On the cubic Nitride of Molybdenum, Soviet Physics - Crystallography. 33 -36.
- [66] R. Sanjinés et al, Valence band photoemission study of the Ti-Mo-N system, Thin Solid Films. 290-291 (1996) 334-338.
- [67] K Saito and Y Asada, Superconductivity and structural changes of nitrogen-ion implanted Mo thin films, Journal of Physics F: Metal Physics. 17 (1987) 2273-2283.
- [68] N. Schönberg, Contributions to the Knowledge of the Molybdenum-Nitrogen and the Tungsten-Nitrogen systems, Acta Chemica Scandinavica. 8 (1954) 204-207.
- [69] K. Inumaru et al, High-Pressure Synthesis of Superconducting Molybdenum Nitride δ -MoN by in Situ Nitridation, Chemistry of Materials. 20 (2008) 4756-4761.
- [70] P. Hones et al, Structural and mechanical properties of chromium nitride, molybdenum nitride, and tungsten nitride thin films, J. Phys. D: Appl. Phys. 36 (2003) 1023-1029.
- [71] E. Soignard et al, High-pressure synthesis and study of low compressibility molybdenum nitride (MoN and MoN_{1-x}) phases, Physical Review B , 132101. 68 (2003).
- [72] C. L. Bull et al, Determination of the crystal structure of δ -MoN by neutron diffraction, Journal of Solid State Chemistry. 177 (2004) 1488-1492.
- [73] L. V. Azároff et al, X-ray diffraction, (1974).
- [74] AJA International Inc, Sputtering - What is Sputtering?
- [75] Newport.com/images.

- [76] J-Y. Lee et al, Effect of deposition conditions on the physical and electrical properties of reactive sputtered molybdenum nitride films, 15 (1996) 1495-1497.
- [77] R. Sanjinés et al, Hexagonal nitride coatings: electronic and mechanical properties of V_2N , Cr_2N and δ -MoN, Thin Solid Films. 332 (1998) 225-229.
- [78] M. A. Nicolet, Diffusion Barriers in Thin Films, Thin Solid Films. 52 (1978) 415-443.
- [79] R. S. Nowiki and I. Wang, Improvement of the diffusion barrier properties of rf-sputtered molybdenum, Journal of Vacuum Science and Technology. 15 (March 1978) 235-237.
- [80] V. P. Anitha et al, Study of sputtered molybdenum nitride as a diffusion barrier, Thin Solid Films. 236 (1993) 306-310.
- [81] J. Lee and J. Park, Diffusion barrier property of Molybdenum Nitride Films for Copper Metallization, Japanese Journal of Applied Physics. 35 (1996) 4280-4284.
- [82] S. Sun and H. Chiu, MOCVD Molybdenum Nitride diffusion barrier for Cu metallization, 09/590,123.
- [83] Petra Alén, Atomic Layer Deposition of TaN, NbN and MoN films for Cu Metallizations, Academic Dissertation, Department of Chemistry, University of Helsinki.
- [84] A. E. Kaloyeros and E. Eisenbraun, Ultrathin Diffusion Barriers/Liners for gigascale copper metallization, Annual Review of Materials. 30 (2000) 363-385.
- [85] M. B. Kanoun et al, Structure and mechanical stability of molybdenum nitrides: A first-principles study, Physical Review B. 76 (2007) 134109.
- [86] Y. Wang, R. Y. Lin, Amorphous molybdenum nitride thin films prepared by reactive sputter deposition, Material Science & Engineering B. 112 (2004) 42-49.
- [87] D. J. Kim, Y. T. Kim, Journal of Applied Physics. 82 (1997) 4847.
- [88] M. Nicolet, Applied Surface Science. 91 (1995) 269.
- [89] Y. J. Lee, B. S. Suh, C.O. Park, Thin Solid Films. 357 (1999) 237.
- [90] H. Matsushashi and S. Nishikawa, Optimum Electrode Materials for Ta_2O_5 Capacitors for High- and Low-Temperature Processes, Japanese Journal of Applied Physics. 33 (1994) 1293-1297.

[91] H-H. Tseng, The Progress and Challenges of Applying High-k/Metal-Gated Devices to Advanced CMOS Technologies, Solid State Circuits Technology.

[92] A. C. Jones, M. L. Hitchman, Chemical Vapour Deposition: Precursors, Processes and Applications.

[93] S-H Wei and S. B. Zhang, NREL, Theoretical Study of Doping Limits of CdTe, NCPV Program Review Meeting.

[94] D. L. Perry and S. L. Phillips, Handbook of Inorganic Compounds.